Available online at www.sciencedirect.com
SCIENCE DIRECT®
Journal of Sound and Vibration 272 (2004) 793–830
JOURNAL OF SOUND AND VIBRATION
www.elsevier.com/locate/jsvi

On the applicability of high-frequency approximations to Lilley's equation

David W. Wundrow[a,*], Abbas Khavaran[b]

[a] Ohio Aerospace Institute, 22800 Cedar Point Road, Brook Park, OH 44142, USA
[b] QSS Group, Inc., 21000 Brookpark Road, Brook Park, OH 44135, USA

Received 17 October 2002; accepted 26 March 2003

Abstract

Three forms of the high-frequency asymptotic Green function for Lilley's equation are reviewed and compared to the exact solution over a wide range of Strouhal numbers. The asymmetric approximation, which applies to sources away from the jet axis, and the quasi-symmetric approximation, which uses a near-axis source assumption, are both obtained for parallel round jets from a formal Fourier-transform solution. The latter of the two is the basis of the so-called MGB computer code (High velocity jet noise source location and reduction, FAA-RD-76-96-II, 1978) and its derivatives. The ray-theory solution, which is the only high-frequency approximation that can be applied to more general mean flows, follows from a WKB ansatz and is shown to be closely related to the asymmetric approximation. The comparisons show that the best overall prediction of the exact Green function is given by the asymmetric approximation which remains accurate down to a Strouhal number of 1/2. The close relationship between the asymmetric and ray-theory approximations suggests that the high-frequency asymptotic Green function for more general mean flows would be similarly successful.

1. Introduction

The prediction of jet noise has been an area of continuous interest over the last half century and has become increasingly important in recent years due to stricter noise regulations placed on the commercial aircraft industry. The need for quieter jet engines has led to several noise abatement techniques such as the placement of tabs and chevrons at the nozzle exit which alter aerodynamic sound generation through enhanced mixing. Accurate and robust prediction tools are

*Corresponding author. Glenn Research Center, Mailstop 5-9 21000, Brookpark Road, Cleveland, OH 44135, USA. Tel.: +1-440-962-3000; fax: +1-440-962-3120.
E-mail address: david.w.wundrow@grc.nasa.gov (D.W. Wundrow).

0022-460X/03/$ - see front matter © 2003 Elsevier Ltd. All rights reserved.
doi:10.1016/S0022-460X(03)00420-6

instrumental in the design of more efficient noise-suppression devices. The present paper considers the applicability of an approximation often made in jet-noise prediction.

Noise generation in jets is generally regarded as a by-product of the unsteady features of the flow and, in many situations of practical interest, the dominant feature is turbulent mixing. Jet-mixing noise emanates from both fine-scale turbulence and the unsteady motions of large-scale coherent structures. The contribution from the latter component is usually most important at shallow angles off the downstream axis (especially in supersonic jets) and is often successfully predicted using either an instability-wave-based approach or a large eddy simulation. It is this noise source that is most directly impacted by mixing enhancement devices since they tend to breakup the large structures at the expense of creating more fine-scale turbulence.

The present investigation is concerned with the mixing noise due to fine-scale turbulence which dominates the spectra away from the downstream jet axis. This component is most often analyzed by employing the acoustic analogy and assuming that the noise generating eddies are compact and behave as convected acoustic sources. The sound field is then governed by Lilley's equation which describes the acoustic propagation on a specified mean flow due to multipole-type sources. The source distribution is, in general, modelled using appropriate space–time correlation functions.

Solutions to Lilley's equation are typically constructed by introducing a Green function. This allows the mean-flow refraction effects to be determined independent of the source distribution and limits the empiricism inherent in the acoustic analogy to the source modelling problem. Despite the linear nature of Lilley's equation, accurate numerical determination of the associated Green function for an arbitrary mean flow is still a major undertaking [1] and consequently much attention has been focused on the simplifications to be gained by use of high-frequency asymptotics [2–4].

The high-frequency limit arises when the acoustic wavelength of the aerodynamic noise is much shorter than the characteristic length scale of the mean flow. For simple round jets, this is usually the case within the first several jet diameters downstream of the nozzle exit where the mixing layer is thin and the turbulence intensity is at its peak. The high-frequency noise can be further increased by the presence of mixing enhancement devices. As a result, high-frequency asymptotic approximations to the Green function for Lilley's equation form the basis of many jet-noise prediction schemes, eg. the so-called MGB computer code [5] and its derivatives.

For arbitrary mean flows, the high-frequency solution to Lilley's equation is described in terms of the ray-theory of acoustics [4]. However, it is often reasonable to assume, for high Reynolds-number jets of practical interest, that the mean flow is both locally parallel and axisymmetric—even jets issuing from tab and chevron nozzles are known to become axisymmetric within 4–5 diameters downstream of the nozzle exit. When the locally parallel and axisymmetric assumption is made, three different closed-form expressions for the high-frequency Green function for Lilley's equation are found in the literature. Goldstein [6] developed an approximation for the Green function by restricting attention to sources located several acoustic wavelengths off the jet axis and determining the high-frequency asymptotics of the formal Fourier-transform solution. Balsa [2,5] also obtained an expression for the high-frequency Green function from the formal Fourier-transform solution but did so by assuming that the source lies near the jet centerline. Finally, Goldstein [3] presented a closed-form ray-theory solution for parallel round jets.

The goal of limiting the empiricism in jet-noise prediction to the source modelling problem will be achieved only when the high-frequency asymptotics provide an accurate approximation of the

exact Lilley's equation Green function. Adequate agreement between the exact source directivity and a high-frequency approximation for Strouhal numbers as small as one has been demonstrated in some limited circumstances by Tester and Morfey [7] for a round jet using a ray-theory solution at polar angles outside the zone of silence and by Scott [8] for a two-dimensional isothermal flow with a piecewise constant mean shear. The primary objective of the present paper is to determine the relative success of the above three high-frequency approximations for parallel round jets by comparing them to the exact order-one frequency solution over a wide range of Strouhal numbers and farfield observation angles. In doing so, the relationships between the different solution forms will be revealed and the potential success of the high-frequency approximation for more general mean flows will be discussed.

The general problem defining the Lilley's equation Green function for a uni-directional transversely sheared mean flow is presented in Section 2 where the formal Fourier-transform solution available for parallel round jets is given. The high-frequency asymptotic behavior of that formal solution is considered in Section 3 where the approximations corresponding to the analyses of Goldstein [6] and Balsa [2,5] are summarized. Appendices A and B provide the details of those analyses with the former correcting an error in the derivation of Goldstein [6]. A comparison of the two high-frequency approximations with the exact order-one frequency Green function is given in Section 4. It is shown there that the best over all prediction of the exact result is provided by the corrected expression of Goldstein which is referred to here as the asymmetric high-frequency approximation and which remains accurate down to a Strouhal number of 1/2. The Balsa expression is referred to as the quasi-symmetric high-frequency approximation and is shown to be at its best when applied to the ring-source directivity in which case it becomes coincident with the asymmetric approximation at sufficiently large polar angles off the downstream jet axis.

The ray-theory solution, which is reviewed for a uni-directional transversely sheared mean flow in Appendix C, is shown to be closely related to the asymmetric high-frequency approximation in Section 5 where the generalization to complex rays in the zone of silence is also considered. In Section 6, local modifications to the ray-theory solution near the caustic and branch point are constructed and a composite solution is presented. The composite ray-theory solution is shown to provide a good approximation to the asymmetric high-frequency solution over the entire range of Strouhal numbers considered and from this result it is inferred that the high-frequency approximation for more general mean flows (i.e., mean flows that are non-axisymmetric and/or non-parallel) would be reasonably accurate down to Strouhal numbers as small as 1/2.

2. Formulation

Interest here is in the acoustic propagation on a parallel, doubly infinite jet for which an exact solution to the steady, inviscid, non-heat-conducting equations of motion is given by

$$\mathbf{u} = \mathbf{i}\bar{u}(y,z), \quad \rho = \bar{\rho}(y,z), \quad c = \bar{c}(y,z), \quad p = \text{constant}, \tag{1}$$

where $\mathbf{u}$, ρ, c and p are the velocity, density, sound speed and pressure respectively. The Cartesian co-ordinates $\mathbf{x} = \{x, y, z\}$ are chosen such that x is aligned with the direction of the mean flow and the unit vector $\mathbf{i}$ is in that direction. The mean-flow profiles are required to approach constant

ambient values,

$$\bar{u}\to 0, \quad \bar{\rho}\to \bar{\rho}_\infty, \quad \bar{c}\to \bar{c}_\infty,$$

as $\sqrt{y^2+z^2}\to\infty$.

Assuming a calorically perfect ideal gas, the linearized equation governing the acoustic propagation on Eqs. (1) is [9]

$$\mathscr{L}\Pi = \frac{\mathrm{D}}{\mathrm{D}t}\left(\frac{\mathrm{D}^2}{\mathrm{D}t^2} - \boldsymbol{\nabla}\cdot\bar{c}^2\boldsymbol{\nabla}\right)\Pi + 2\bar{c}^2\boldsymbol{\nabla}\bar{u}\cdot\boldsymbol{\nabla}\frac{\partial}{\partial x}\Pi = \Gamma, \tag{2}$$

where Π denotes the acoustic pressure fluctuation normalized by $\bar{\rho}\bar{c}^2$,

$$\frac{\mathrm{D}}{\mathrm{D}t} \equiv \frac{\partial}{\partial t} + \bar{u}\frac{\partial}{\partial x}$$

is the convective derivative relative to the mean flow and t denotes the time. The term Γ represents the acoustic source distribution and is given by

$$\Gamma = \frac{\mathrm{D}}{\mathrm{D}t}\boldsymbol{\nabla}\cdot\mathbf{f} - 2\boldsymbol{\nabla}\bar{u}\cdot\frac{\partial}{\partial x}\mathbf{f}, \tag{3}$$

when produced by a fluctuating force per unit volume. In the absence of temperature fluctuations, Lilley's equation [10] is obtained by replacing $\mathbf{f}$ with the quadrupole source distribution $\mathbf{f} = \boldsymbol{\nabla}\cdot(\mathbf{v}\otimes\mathbf{v})$ where $\mathbf{v}$ is the velocity fluctuation relative to the mean flow and $\otimes$ denotes the tensor product.

Since Eq. (2) is linear, the solution for an arbitrary source distribution can be obtained through superposition of solutions to

$$\mathscr{L}[G_\omega(\mathbf{x}|\mathbf{x}_\mathrm{s})\mathrm{e}^{-\mathrm{i}\omega t}] = \frac{\mathrm{D}}{\mathrm{D}t}[\bar{c}_\infty^2\,\delta(\mathbf{x}-\mathbf{x}_\mathrm{s})\mathrm{e}^{-\mathrm{i}\omega t}], \tag{4}$$

where ω is the frequency, $\mathbf{x}_\mathrm{s}$ is the source position, δ is the Dirac delta function and G_ω denotes a reduced Green function. It is common practice to include the convective derivative $\mathrm{D}/\mathrm{D}t$ in the inhomogeneous term of the reduced Green function equation because doing so simplifies the subsequent computation of the acoustic field when attention is restricted to the first term in Eq. (3)—the so-called self-noise term. It should be noted however that use of Eq. (4) does not limit the form of Γ since the reduced Green function $\mathbb{G}_\omega$ corresponding to the right-hand side,

$$\bar{c}_\infty^2\,\delta(\mathbf{x}-\mathbf{x}_\mathrm{s})\mathrm{e}^{-\mathrm{i}\omega t},$$

is related to G_ω by

$$G_\omega(\mathbf{x}|\mathbf{x}_\mathrm{s}) = -\left(\mathrm{i}\omega + \bar{u}_\mathrm{s}\frac{\partial}{\partial x_\mathrm{s}}\right)\mathbb{G}_\omega(\mathbf{x}|\mathbf{x}_\mathrm{s}), \tag{5}$$

where the subscript s denotes evaluation at the source position.

When the mean flow depends only on the radial co-ordinate in the y–z plane $r \equiv \sqrt{y^2+z^2}$, a formal solution for G_ω can be obtained by reducing Eq. (4) to a system of linear ordinary differential equations. Following Goldstein [6], the reduced Green function is written as

$$G_\omega(\mathbf{x}|\mathbf{x}_\mathrm{s}) = \frac{1}{4\pi^2}\sum_{n=-\infty}^{+\infty}\mathrm{e}^{\mathrm{i}n(\varphi-\varphi_\mathrm{s})}\int_{-\infty}^{+\infty} G_n(r|r_\mathrm{s};\omega,k_1)\mathrm{e}^{-\mathrm{i}k_1(x-x_\mathrm{s})}\,\mathrm{d}k_1, \tag{6}$$

where $\varphi \equiv \arctan(z/y)$ is the azimuthal angle in the y–z plane. The Fourier coefficients G_n are determined by

$$\frac{\Phi^2}{r}\frac{\mathrm{d}}{\mathrm{d}r}\left(\frac{r}{\Phi^2}\frac{\mathrm{d}}{\mathrm{d}r}G_n\right) + \left[k_0^2(\Phi^2-\kappa^2) - \frac{n^2}{r^2}\right]G_n = -\frac{\delta(r-r_\mathrm{s})}{ra^2}, \tag{7}$$

where $\Phi \equiv (1+\kappa M)/a$, $k_0 \equiv \omega/\bar{c}_\infty$, $\kappa \equiv k_1/k_0$, $a \equiv \bar{c}/\bar{c}_\infty$ is the local sound speed normalized by its ambient value and $M \equiv \bar{u}/\bar{c}_\infty$ is the local Mach number based on the ambient speed of sound.

Eq. (7) must be solved subject to the conditions that G_n remains bounded at $r = 0$ and behaves like an outgoing wave as $r \to \infty$. The solution satisfying these conditions can be expressed in terms of two linearly independent homogeneous solutions to Eq. (7), say w_1 and w_2, as follows [11]:

$$G_n(r|r_\mathrm{s};\omega,k_1) = \frac{w_1(r|\kappa)w_2(r_\mathrm{s}|\kappa)}{r_\mathrm{s}a_\mathrm{s}^2 W(r_\mathrm{s}|\kappa)} \quad \text{for } r > r_\mathrm{s}, \tag{8}$$

where

$$W(r|\kappa) \equiv w_1(r|\kappa)w_2'(r|\kappa) - w_1'(r|\kappa)w_2(r|\kappa)$$

is the Wronskian, a prime denotes differentiation with respect to r and the w_j have been chosen such that

$$w_1 \to \text{constant} \times r^{-1/2}\mathrm{e}^{\mathrm{i}k_0\sqrt{1-\kappa^2}r} \quad \text{as } r \to \infty, \tag{9}$$

$$w_2 \to \text{constant} \times r^{|n|} \quad \text{as } r \to 0. \tag{10}$$

Only the $r > r_\mathrm{s}$ form of G_n is given since primary interest is in the behavior of the solution in the far field.

The homogeneous solutions w_j must be determined numerically in general. However, when the frequency is sufficiently large, the equations become simple enough to be solved analytically.

3. High-frequency, farfield approximation

The high-frequency limit describes the situation wherein the wavelength of the acoustic field, $1/k_0 = \bar{c}_\infty/\omega$, is much shorter than the characteristic length scale of the mean flow, viz. the jet radius

$$r_J \equiv \frac{1}{M_J}\int_0^\infty \frac{\bar{u}(r)}{\bar{c}(r)}\,\mathrm{d}r = \frac{1}{M_J}\int_0^\infty \frac{M(r)}{a(r)}\,\mathrm{d}r, \tag{11}$$

where M_J is a jet Mach number which is taken here to be the ratio of the axial velocity to the *local* speed of sound at the jet centerline. The streamwise wavelength $1/k_1$ scales like $1/k_0$ in the present analysis and the high-frequency limit can therefore be expressed mathematically as

$$\frac{\omega}{\bar{c}_\infty} = k_0 \to \infty, \quad \text{with } \frac{k_1}{k_0} = \kappa = O(1),$$

where it has been assumed, for simplicity, that the mean-flow quantities M, a and r_J are all order one.

In many technological applications, one is only interested in the behavior of the acoustic field at remote distances (in terms of the characteristic mean-flow length scale) from the aerodynamic noise sources. The so-called farfield behavior is most conveniently expressed by introducing polar co-ordinates in the x–r plane,

$$R = \sqrt{(x - x_s)^2 + (r - r_s)^2}, \quad \theta = \arccos\left(\frac{x - x_s}{R}\right),$$

with origin at the source position, and considering the limit as $R \to \infty$.

Using Eq. (9), it can be shown that the integrand in Eq. (6) has a point of stationary phase at

$$\kappa = -\cos\theta + O(R^{-1}),$$

as $R \to \infty$. The integral over k_1 can then be approximated using the method of stationary phase [11] with the result that

$$\int_{-\infty}^{+\infty} G_n(r|r_s;\omega,k_1)\mathrm{e}^{-\mathrm{i}k_1(x-x_s)}\mathrm{d}k_1$$
$$\sim \left(\frac{2\pi k_0 \sin^2\theta}{\mathrm{i}R}\right)^{\frac{1}{2}} \frac{w_1(r|-\cos\theta)w_2(r_s|-\cos\theta)}{r_s a_s^2 W(r_s|-\cos\theta)}\,\mathrm{e}^{\mathrm{i}k_0 R\cos^2\theta} \tag{12}$$

as $k_0, R \to \infty$.

The asymptotic approximation for G_ω is completed by determining the high-frequency behavior of w_1 and w_2. To facilitate this, new dependent variables v_1 and v_2 are introduced as follows:

$$w_j(r|-\cos\theta) = \frac{\Phi(r)}{\sqrt{r}} v_j(r) \quad \text{for } j = 1, 2,$$

where now $\Phi = (1 - M\cos\theta)/a$. Substituting into Eqs. (7), (9) and (10) shows that the v_j must satisfy

$$v'' + (k_0^2 Q_n^2 + \mathscr{S})v = 0 \tag{13}$$

subject to

$$v_1 \to \text{constant} \times \mathrm{e}^{\mathrm{i}k_0 r\sin\theta} \quad \text{as} \quad r \to \infty, \tag{14}$$

$$v_2 \to \text{constant} \times r^{1/2+|n|} \quad \text{as} \quad r \to 0, \tag{15}$$

where

$$rQ_n(r) \equiv \sqrt{r^2 q^2 - (n/k_0)^2}, \quad q(r) \equiv \sqrt{\Phi^2 - \cos^2\theta}, \tag{16}$$

$$\mathscr{S}(r) \equiv \frac{\Phi}{r}\left(\frac{r\Phi'}{\Phi^2}\right)' + \left(\frac{1}{2r}\right)^2, \tag{17}$$

and the square roots in Eq. (16) are chosen such that they have positive imaginary parts for negative arguments. Introducing v_1 and v_2 into Eq. (12) and the result into Eq. (6) leads to

$$G_\omega(\mathbf{x}|\mathbf{x}_s) \sim \frac{\mathscr{G}_\omega(\mathbf{x}|\mathbf{x}_s)\mathscr{R}_\omega(\mathbf{x}|\mathbf{x}_s)}{a_s(1 - M_s\cos\theta)}, \tag{18}$$

as $k_0, R \to \infty$, where

$$\mathscr{G}_\omega(\mathbf{x}|\mathbf{x}_s) \equiv \frac{e^{ik_0 R}}{4\pi R}, \tag{19}$$

corresponds to the reduced free-space Green function when both the source and farfield observation points lie in the same azimuthal plane,

$$\mathscr{R}_\omega(\mathbf{x}|\mathbf{x}_s) \equiv \sum_{n=-\infty}^{+\infty} \left(\frac{2k_0 \sin\theta}{i\pi r_s}\right)^{1/2} \frac{v_1(r)v_2(r_s)}{V} e^{in\Delta\varphi - ik_0 R\sin^2\theta}, \tag{20}$$

$\Delta\varphi \equiv \varphi - \varphi_s$ and $V \equiv v_1 v_2' - v_1' v_2$ is the Wronskian which, in view of Eq. (13), is independent of r.

Before the high-frequency asymptotic solutions to Eq. (13) can be constructed, the scaling of the azimuthal wavenumber n with k_0 must be considered. The summation in Eq. (20) suggests the need for uniformly valid approximations to v_1 and v_2 for all n. However, the dominant behavior of G_ω in the limit as $k_0 \to \infty$ is determined by a relatively small number of azimuthal modes centered about a critical value of n and it suffices to construct asymptotic solutions to Eq. (13) based on the k_0 scaling of that critical value.

When the distance between the source and jet axis is sufficiently large (i.e., several factors of $1/k_0$), the resulting acoustic field is asymmetric and the critical azimuthal wavenumber behaves like the streamwise wavenumber and scales with k_0. This scaling was considered by Goldstein [6] and will be referred to as the asymmetric, high-frequency approximation. As the source moves closer to the jet axis the acoustic field becomes increasingly symmetric and eventually the critical value of n scales like $1/r_J$. The near-axis source problem was analyzed by Balsa [2,5] and will be referred to here as the quasi-symmetric, high-frequency approximation.

Solutions to Eq. (13) using the asymmetric, high-frequency scaling,

$$n = O(k_0) \quad \text{as} \quad k_0 \to \infty,$$

were constructed by Goldstein [6], however, the bounded solution used in that analysis (Eq. (6.61) of Ref. [6]) needs correction. The correct asymptotic solutions for v_1 and v_2 are given in Appendix A. Using those results in Eq. (20) leads to

$$\mathscr{R}_\omega \sim \sum_{n=-\infty}^{+\infty} \left[\frac{2}{k_0} \frac{\sqrt{-\eta_n(r_s)}}{r_s Q_n(r_s)}\right]^{1/2} \mathrm{Ai}[\eta_n(r_s)] e^{in\Delta\varphi + ik_0(\zeta_n - R\sin^2\theta)}, \tag{21}$$

as $k_0, R \to \infty$, where

$$\eta_n(r) \equiv -\left[\frac{3}{2} k_0 \zeta_n(r)\right]^{2/3}, \quad \zeta_n(r) \equiv \int_{r_\delta}^{r} Q_n(r)\,dr, \quad Q_n^2(r_\delta) = 0,$$

Ai denotes the Airy function and the cube root in the definition of η_n is taken such that $\eta_n \lessgtr 0$ for $r \gtrless r_\delta$. Notice that the outgoing-wave solution v_1 and the Wronskian V have been replaced by their high-frequency, farfield approximations in arriving at Eq. (21). The evaluation of the summands is then reduced to determining the bounded solution v_2 at the source position which can be done either analytically as in Eq. (21) or numerically by integrating Eq. (13) from $r \to 0$ to $r = r_s$ subject to initial conditions derived from Eq. (15) and the normalizations (A.2) and (A.3).

Solutions to Eq. (13) using the quasi-symmetric, high-frequency scaling,

$$n = O(1) \quad \text{as} \quad k_0 \to \infty,$$

are given in Appendix B. Substituting Eqs. (B.5) into (20) yields

$$\mathscr{R}_\omega \sim \sum_{n=-\infty}^{+\infty} \sqrt{\mathrm{i}\tfrac{1}{2}\pi k_0 \xi}\, \mathrm{H}_n^{(1)}(k_0\xi)\mathrm{J}_n(k_0\xi_\mathrm{s})\mathrm{e}^{\mathrm{i}n\Delta\varphi - \mathrm{i}k_0 R\sin^2\theta}, \tag{22}$$

as k_0, $R \to \infty$, where

$$\xi(r) \equiv \int_0^r q(r)\,\mathrm{d}r = \zeta_0(r) - \zeta_0(0),$$

$\mathrm{H}_n^{(1)}$ and J_n denote the Hankel and Bessel functions of the first kind, respectively, and the quantity under the square root has been simplified by making the approximation $\xi_\mathrm{s} \approx r_\mathrm{s} q_\mathrm{s}$ which was also used in Ref. [5] and becomes increasingly accurate as $r_\mathrm{s} \to 0$.

One advantage of the quasi-symmetric approximation is that the sum over n in Eq. (22) can be evaluated in closed form. Using Graf's addition theorem [12], one can write

$$\sum_{n=-\infty}^{+\infty} \mathrm{H}_n^{(1)}(k_0\xi)\mathrm{J}_n(k_0\xi_\mathrm{s})\mathrm{e}^{\mathrm{i}n\Delta\varphi} = \mathrm{H}_0^{(1)}\left(k_0\sqrt{\xi^2 + \xi_\mathrm{s}^2 - 2\xi\xi_\mathrm{s}\cos\Delta\varphi}\right),$$

which, when substituted into Eq. (22), leads to

$$\mathscr{R}_\omega \sim \mathrm{e}^{\mathrm{i}k_0(\xi - R\sin^2\theta - \xi_\mathrm{s}\cos\Delta\varphi)}, \tag{23}$$

as k_0, $R \to \infty$, where $\mathrm{H}_0^{(1)}$ has been replaced by its large argument behavior since $\xi \to \infty$ in the limit $R \to \infty$.

4. Comparison of exact and asymptotic solutions

Comparisons of the high-frequency, farfield approximations to the exact solution for the reduced Green function are most easily carried out in terms of $\mathbb{G}_\omega$. It follows from Eqs. (5) and (18) that

$$\mathbb{G}_\omega(\mathbf{x}|\mathbf{x}_\mathrm{s}) \sim \frac{\mathrm{i}G_\omega(\mathbf{x}|\mathbf{x}_\mathrm{s})}{\omega(1 - M_\mathrm{s}\cos\theta)} \sim \frac{\mathrm{i}\mathscr{G}_\omega(\mathbf{x}|\mathbf{x}_\mathrm{s})\mathscr{R}_\omega(\mathbf{x}|\mathbf{x}_\mathrm{s})}{\omega a_\mathrm{s}(1 - M_\mathrm{s}\cos\theta)^2}, \tag{24}$$

as $k_0, R \to \infty$, where $\mathscr{R}_\omega$ is given by Eqs. (21) or (23) for the asymmetric or quasi-symmetric approximation respectively. The exact solution for $\mathbb{G}_\omega$ is obtained numerically using the adjoint Green function scheme given by Tam and Auriault [13]. The interested reader is referred to that reference for the details.

The mean-flow Mach number profile used in the comparisons is

$$\frac{\bar{u}(r)}{\bar{c}(r)} = \frac{M(r)}{a(r)} = M_J \mathrm{sech}^2(2r), \tag{25}$$

and it follows from Eq. (11) that the jet radius $r_J = 1/2$. The profile is shown in Fig. 1 for a jet Mach number $M_J = 0.9$.

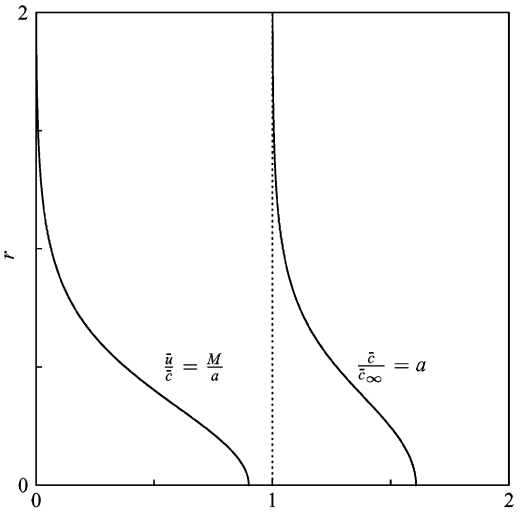

Fig. 1. Mean-flow profiles (25) and (28) with $M_J = 0.9$ and $T_R = 3$.

Two different profiles are considered for the sound speed ratio a. The first corresponds to an isothermal jet which, in view of the ideal-gas result

$$\bar{c} = \sqrt{\gamma \Re T}, \tag{26}$$

has a constant speed of sound and therefore

$$a(r) = 1, \tag{27}$$

where γ is the ratio of specific heats, $\Re$ is the gas constant and T is the mean static temperature. The second profile is obtained from Eq. (26) and the Crocco–Busemann law and is given by

$$a^2(r) = 1 + \left(1 + \frac{\gamma - 1}{2} M_J^2\right)^{1/2} \frac{T_R - 1}{M_J \sqrt{T_R}} M(r) - \frac{\gamma - 1}{2} M^2(r), \tag{28}$$

where

$$T_R \equiv \left(1 + \frac{\gamma - 1}{2} M_J^2\right) \frac{T_J}{T_\infty}$$

is the ratio of the stagnation temperature at the jet centerline to the ambient temperature. In the results presented here, $\gamma = 1.4$, $\Re = 287.06$ J/kg K and $T_\infty = 290$ K. The a profile obtained from Eqs. (25) and (28) with $M_J = 0.9$ and $T_R = 3$ is shown in Fig. 1.

In deriving the asymmetric, high-frequency approximation (21), it was assumed (see Appendix A) that, for each order-k_0 value of n, Eq. (13) has one simple turning point r_δ corresponding to a zero of Q_n^2. Fig. 2(a) is a plot of $r^2 q^2$ for various polar angles θ using Eqs. (25) and (27) with $M_J = 0.9$. Similar curves are obtained for hot jets with a given by Eq. (28). Since the zeroes of Q_n^2 are determined by solutions to

$$r^2 q^2 = (n/k_0)^2, \tag{29}$$

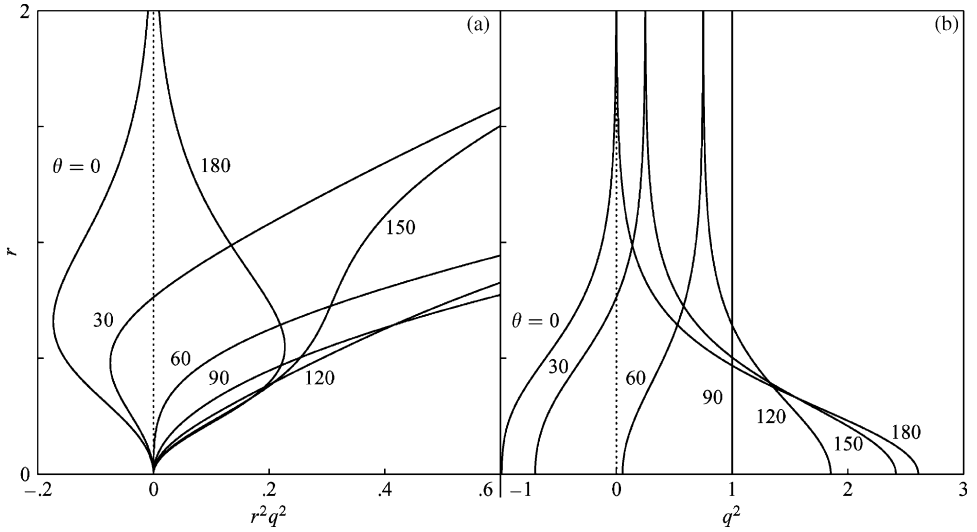

Fig. 2. Turning point functions for an isothermal jet at various θ.

Fig. 2(a) shows that the turning-point assumption made in Appendix A holds for $0^\circ < \theta \leqslant 150^\circ$ provided $n/k_0 \neq 0$. For $\theta > 150^\circ$, multiple turning points are possible for certain values of n/k_0. This behavior can be accounted for by making appropriate modifications to the analysis in Appendix A; however, these upstream angles are usually of no practical interest and will not be considered here.

The curves in Fig. 2(a) show that the turning-point assumption of Appendix A is violated when $n = 0$ and $\theta \gtrsim 58^\circ$ in which case Eq. (29) has no real solution for r_δ (see also Fig. 2(b)). Since the azimuthal wavenumber scaling $n = O(k_0)$ clearly does not apply to the $n = 0$ term in Eq. (20), it would seem that this term must be evaluated using the $n = O(1)$ scaling of the *quasi-symmetric* approximation. However, if the convention that $r_\delta = 0$ when Q_n^2 has no zeroes is adopted (as is done for r_σ in Appendix B), Eqs. (A.4) and (B.5) can be shown to agree at $n = 0$ by simply replacing the functions Ai, $\mathrm{H}_0^{(1)}$ and J_0 appearing in these expressions by their large argument behaviors. The same proof also applies when Q_0^2 has a zero provided the simplifying assumption $r_\delta - r_s \gg k_0^{-2/3}$ of Appendix B is made. It therefore follows that the results of Appendix A remain valid even when $n = 0$.

The quasi-symmetric analysis of Appendix B is based on the assumption that Eq. (B.2) has at most one simple turning point r_σ corresponding to a zero of q^2. Fig. 2(b) is a plot of q^2 for various angles θ and the same isothermal mean-flow profiles used in part (a). Again, similar curves were found for heated jets. It is clear from the figure that q^2 has one simple zero for $0^\circ < \theta \lesssim 58^\circ$ and none for $\theta \gtrsim 58^\circ$. At $\theta \approx 58^\circ$, q^2 has a higher order zero at $r = 0$ which was not accounted for in the analysis of Appendix B. The effect of this omission is highly localized and, apart from a small neighborhood of $\theta \approx 58^\circ$, the turning point assumption of Appendix B is satisfied for the entire range of polar angles considered here.

4.1. Point-source results

When comparing the exact and asymptotic solutions for $\mathbb{G}_\omega$, it is convenient to work in terms of the ratio $\mathbb{G}_\omega/\mathscr{G}_\omega$ since this quantity becomes independent of the radial parameter R in the high-frequency, farfield limit. Figs. 3–6 show $|\mathbb{G}_\omega/\mathscr{G}_\omega|$ as a function of the polar angle θ for various values of the Strouhal number,

$$St \equiv \frac{\omega}{2\pi}\frac{2r_J}{\bar{c}_\infty a(0)M_J} = \frac{k_0}{\pi}\frac{r_J}{a(0)M_J}.$$

Parts (a–d) of each figure correspond to azimuthal-angle parameters $\Delta\varphi$ of 0°, 30°, 90° and 120°. The asymmetric and quasi-symmetric approximations are indicated by the solid and dashed lines,

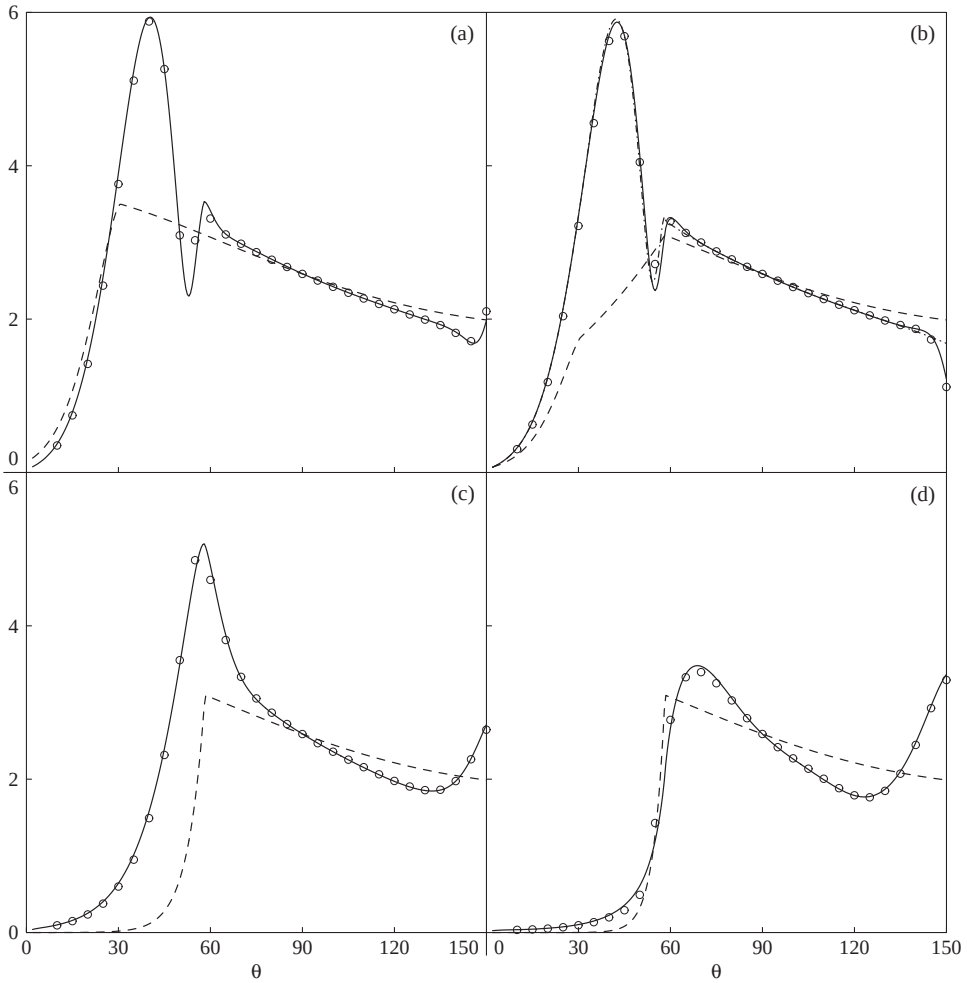

Fig. 3. $|\mathbb{G}_\omega/\mathscr{G}_\omega| \times 10^4$ for an isothermal jet with $r_s = 0.75$ and $St = 2$. Solid lines, asymmetric approximation; dashed lines, quasi-symmetric approximation; symbols, exact solution. (a) $\Delta\varphi = 0°$; (b) $\Delta\varphi = 30°$, dot-dashed line, composite ray solution; (c) $\Delta\varphi = 90°$; (d) $\Delta\varphi = 120°$.

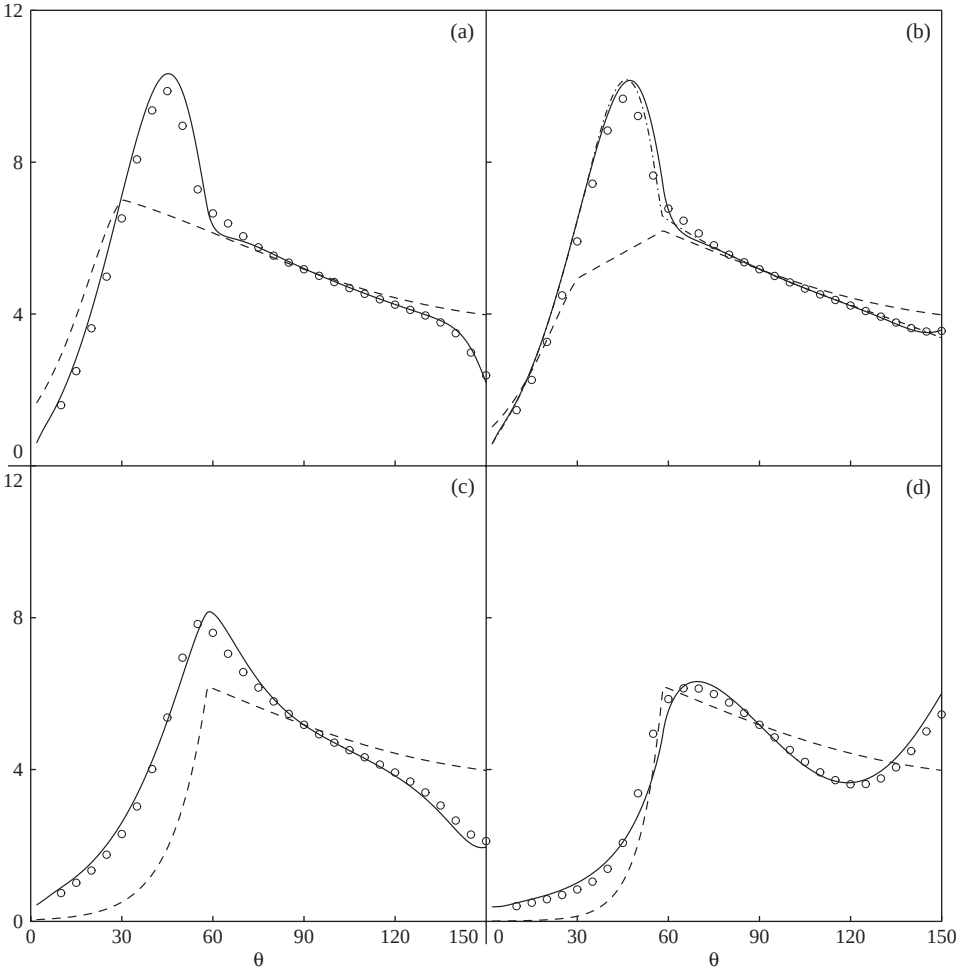

Fig. 4. As Fig. 3 but for $St = 1$.

respectively, and the symbols correspond to the exact solution. The asymmetric approximation given by Eq. (21) was evaluated by summing the convergent series in the azimuthal wavenumber n from $-N$ to $+N$ where N varied from 11 at $St = 2$ down to 4 at $St = 0.25$. The results in Figs. 3–6 were computed for a point source at $r_s = 0.75$ using a mean flow given by Eqs. (25) and (27) with $M_J = 0.9$.

Fig. 3 shows excellent agreement between the asymmetric approximation and the exact result for all $\Delta\varphi$. The level of agreement tends to diminish as St decreases but remains fairly good down to $St = 0.5$, cf. Fig. 5. At the smallest Strouhal number (cf. Fig. 6), the asymmetric approximation, although no longer in good quantitative agreement, does still correctly predict the trends of the exact solution—a peak near $\theta = 60^\circ$ with a steep drop off for $\theta < 60^\circ$ and a more gradual decline for $\theta > 60^\circ$.

Figs. 3–6 show that, at $\theta = 90^\circ$, both the asymmetric and quasi-symmetric approximations remain in near perfect agreement with the exact solution for all St. At $\theta = 90^\circ$, the mean-flow

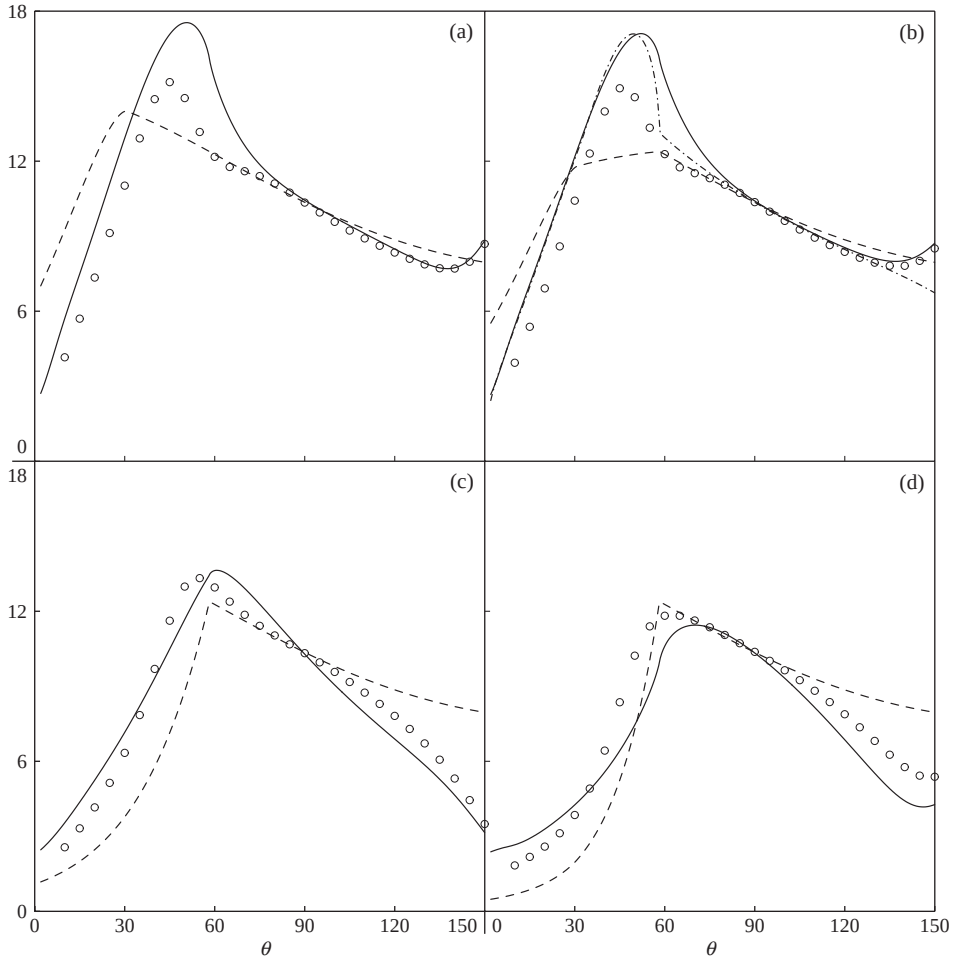

Fig. 5. As Fig. 3 but for $St = 0.5$.

refraction effects for an isothermal jet vanish as can be readily verified from the expression for Φ. It is interesting to note that this exceptional case is captured equally well by both high-frequency approximations despite their differences in assumed azimuthal wavenumber scaling.

Considering the quasi-symmetric approximation, the most striking feature revealed by Figs. 3–6 is the failure to predict the oscillatory behavior of the exact solution in the range $30^\circ < \theta < 60^\circ$. This is due in large part to the assumption introduced in reference [2] (and used in Appendix B) that the no-turning-point form of G_ω adequately approximates the Green function when $r_s > r_\sigma > 0$. It can be seen from Fig. 2(b) that Eq. (B.2) has a turning point that lies between the source position $r_s = 0.75$ and the jet axis when $30^\circ < \theta < 60^\circ$. By neglecting the turning point, the quasi-symmetric approximation does not allow for ray-interference effects which are primarily responsible for the oscillations in the exact solution (cf. Section 6).

The figures also show that, in the range $\theta < 30^\circ$, the quasi-symmetric approximation tends to over predict $|\mathbb{G}_\omega/\mathscr{G}_\omega|$ when $\Delta\varphi < 90^\circ$ and under predicts this quantity when $\Delta\varphi > 90^\circ$. For $\theta > 60^\circ$,

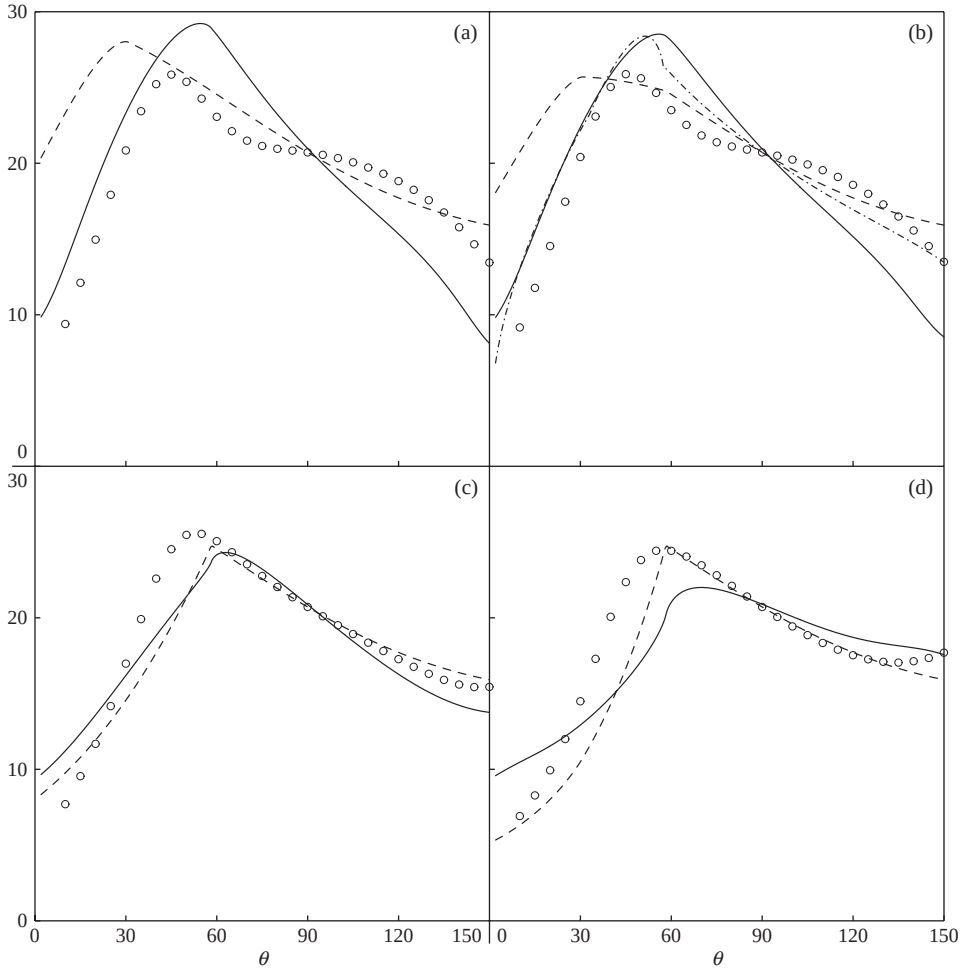

Fig. 6. As Fig. 3 but for $St = 0.25$.

the agreement between the quasi-symmetric approximation and the exact solution actually improves as St decreases. This surprising behavior, which was also noted by Balsa [2], is probably due to the increase in acoustic length scale with decreasing Strouhal number which, for a fixed source position, makes the solution appear more axisymmetric. It should also be noted that the ray-interference effects near $\theta = 60^\circ$ diminish as St decreases and this too improves the agreement with the exact solution.

When modelling the acoustic-source distribution Γ for use in a noise prediction scheme, it is usual to assume that the sources are sufficiently compact so that only the absolute value of $\mathbb{G}_\omega$ appears in the resulting formulae. Nevertheless, it may be of some interest to see how well the high-frequency, farfield approximations predict the phase of $\mathbb{G}_\omega/\mathscr{G}_\omega$. This quantity is plotted in Fig. 7 at $St = 1$ for various $\Delta\varphi$ and the same mean flow used for Figs. 3–6. The curves show that overall the asymmetric approximation is better than the quasi-symmetric approximation at

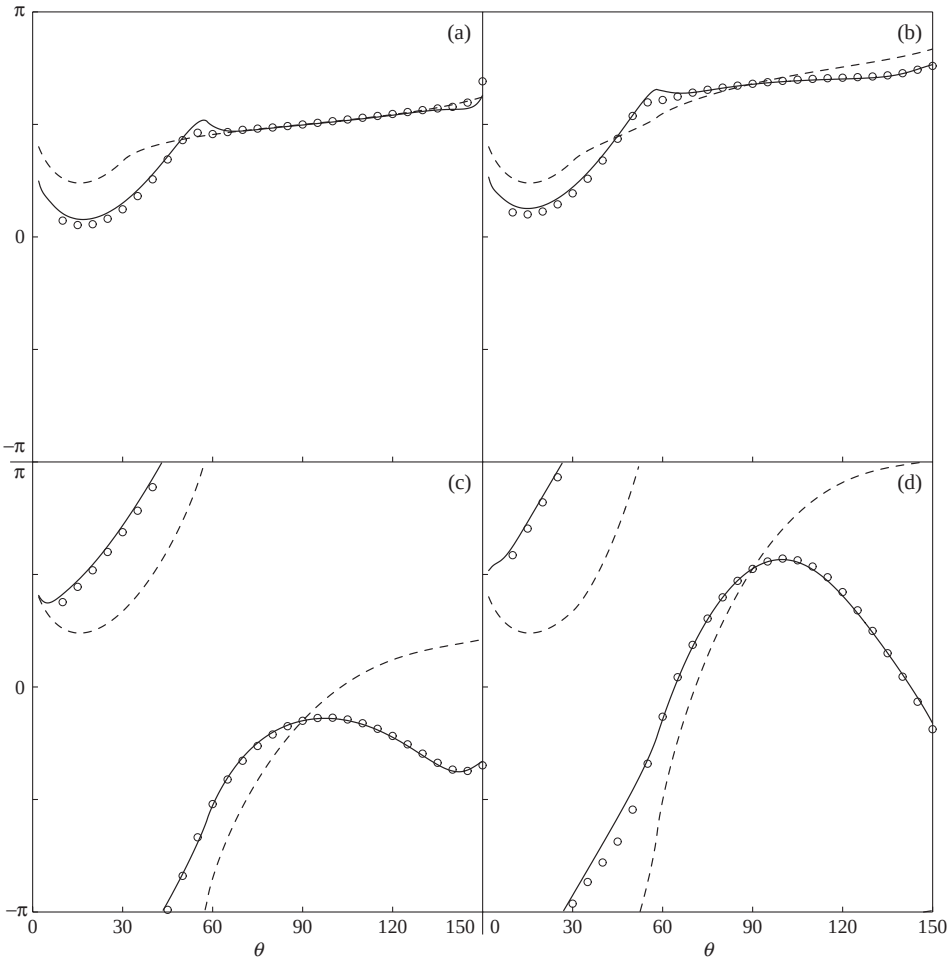

Fig. 7. $\arg(\mathbb{G}_\omega/\mathscr{G}_\omega)$ for an isothermal jet with $r_s = 0.75$ and $St = 1$. Solid lines, asymmetric approximation; dashed lines, quasi-symmetric approximation; symbols, exact solution. (a) $\Delta\varphi = 0^\circ$; (b) $\Delta\varphi = 30^\circ$; (c) $\Delta\varphi = 90^\circ$; (d) $\Delta\varphi = 120^\circ$.

predicting the exact result. The quasi-symmetric approximation is at its best when $\Delta\varphi < 90^\circ$ and $\theta > 45^\circ$.

4.2. Ring-source results

In the case of round jets, it is often also assumed that the strength and orientation of the sound sources that make up Γ are independent of the azimuthal angle. The sound field emitted by such a source distribution is then axisymmetric and, at fixed axial and radial positions, can be characterized by a ring-source directivity factor which is defined here as

$$\mathscr{D} \equiv \int_{-\pi}^{+\pi} \left|\frac{\mathbb{G}_\omega}{\mathscr{G}_\omega}\right|^2 \mathrm{d}\varphi_s, \sim \frac{1}{\omega^2 a_s^2 (1 - M_s \cos\theta)^4} \int_{-\pi}^{+\pi} |\mathscr{R}_\omega|^2 \,\mathrm{d}\varphi_s,$$

as $k_0, R \to \infty$. It follows from Eq. (21) that

$$\int_{-\pi}^{+\pi} |\mathscr{R}_\omega|^2 \, \mathrm{d}\varphi_\mathrm{s} \sim \frac{4\pi}{k_0} \sum_{n=-\infty}^{+\infty} \frac{\sqrt{-\eta_n(r_\mathrm{s})}}{r_\mathrm{s} Q_n(r_\mathrm{s})} \mathrm{Ai}^2[\eta_n(r_\mathrm{s})], \tag{30}$$

for the asymmetric approximation, and from Eq. (23) that

$$\int_{-\pi}^{+\pi} |\mathscr{R}_\omega|^2 \, \mathrm{d}\varphi_\mathrm{s} \sim 2\pi \mathrm{e}^{-2k_0 \, \mathrm{Im} \, \xi_\sigma} \mathrm{I}_0(2k_0 \, \mathrm{Im} \, \xi_\mathrm{s}) \approx 2\pi \mathrm{e}^{-2k_0 \, \mathrm{Im}(\xi_\sigma - \xi_\mathrm{s})}, \tag{31}$$

for the quasi-symmetric approximation, as $k_0, R \to \infty$, where I_0 denotes the modified Bessel function of the first kind and zeroth order and a subscript σ indicates evaluation at the turning point $r = r_\sigma$. The approximation introduced on the far right-hand side of Eq. (31) corresponds to a leading-order composite expansion for the ring-source directivity and puts the quasi-symmetric approximation in agreement with the relation used in the so-called MGB computer code of Ref. [5].

The ring-source directivity factor is plotted as a function of polar angle θ in Figs. 8–11 for Strouhal numbers $St = 2$, 1, 0.5 and 0.25. Parts (a) and (b) of each figure correspond to the mean flow given by Eqs. (25) and (27) with $M_J = 0.9$ but differing source positions, $r_\mathrm{s} = 0.5$ and 0.75 respectively. Similarly, parts (c) and (d) show results at $r_\mathrm{s} = 0.5$ and 0.75, respectively, for the heated jet given by Eqs. (25) and (28) with $M_J = 0.9$ and $T_R = 3$.

The figures show that the agreement between the asymmetric approximation and the exact result is excellent at $St = 2$ and remains good down to $St = 0.5$. Even at $St = 0.25$, the approximation does a fair job at predicting the exact result for $\theta > 60^\circ$ which corresponds to the range where the jet noise is dominated by fine-scale turbulence in many technological applications. At the two largest Strouhal numbers, the level of agreement shows no sensitivity to changes in the source radius or mean-flow temperature profile. A sensitivity to the source radius becomes apparent at the two lowest St but only in the range $\theta < 60^\circ$. This may indicate an increased importance of the $n = 0$ term in Eq. (30) as the source moves toward the jet centerline.

The agreement between the quasi-symmetric approximation and the exact solution is best when $\theta > 60^\circ$ regardless of St. In this range, the quasi-symmetric and asymmetric ring-source approximations are nearly coincident—a result that is not simply fortuitous. By approximating the sum in Eq. (30) with a Riemann integral [11] and then determining the large-k_0 behavior of that integral assuming the dominant contribution comes from the range where $r_\mathrm{s} - r_\delta \gg k_0^{-2/3}$, it can be shown that the right-hand side of Eq. (30) approaches 2π as $k_0 \to \infty$ in exact agreement with the quasi-symmetric approximation (31).

For $\theta < 60^\circ$, the quasi-symmetric approximation is never very good, primarily because of a consistent under prediction of the θ at which $\mathscr{D}$ is a maximum. This may indicate the increased importance of asymmetric effects when the Green function problem possesses a turning point. A conjecture that is supported by the worsening agreement in the downstream range $\theta < 90^\circ$ for the heated jet which, it turns out, has a broader range of θ where a turning point arises. The agreement between the quasi-symmetric and asymmetric approximations observed for $\theta > 60^\circ$ is absent at small θ due to a difference in respective amplitude functions. When θ is such that the dominant contribution to the Riemann-integral approximation comes from the range where

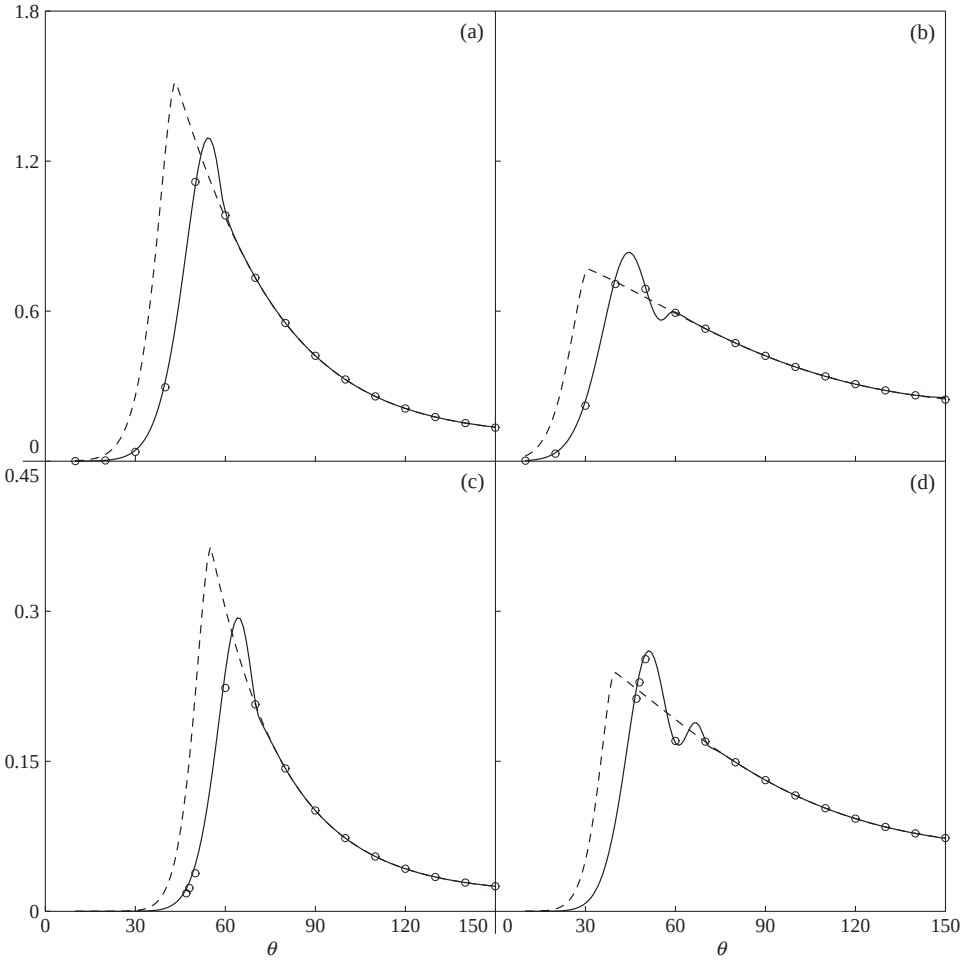

Fig. 8. Ring-source directivity $\mathscr{D} \times 10^6$ for isothermal (a,b) and heated (c, d) jets at $St = 2$. Solid lines, asymmetric approximation; dashed lines, quasi-symmetric approximation; symbols, exact solution. (a, c), $r_s = 0.5$; (b, d), $r_s = 0.75$.

$r_\delta - r_s \gg k_0^{-2/3}$, the right-hand side of Eq. (30) becomes

$$\left[-\frac{k_0}{\pi} \int_{r_s}^{r_\sigma} \frac{r_s^2 q_s^2}{r^2 \sqrt{-q^2}} \, \mathrm{d}r \right]^{-1/2} \mathrm{e}^{-2k_0 \mathrm{Im}(\xi_\sigma - \xi_s)}$$

as $k_0 \to \infty$. The above result is only accurate for $\theta < 20^\circ$ and becomes unbounded when θ is such that q_s^2 vanishes. An analogous breakdown occurs in the amplitude function obtained from ray theory and is considered in more detail in Section 6.

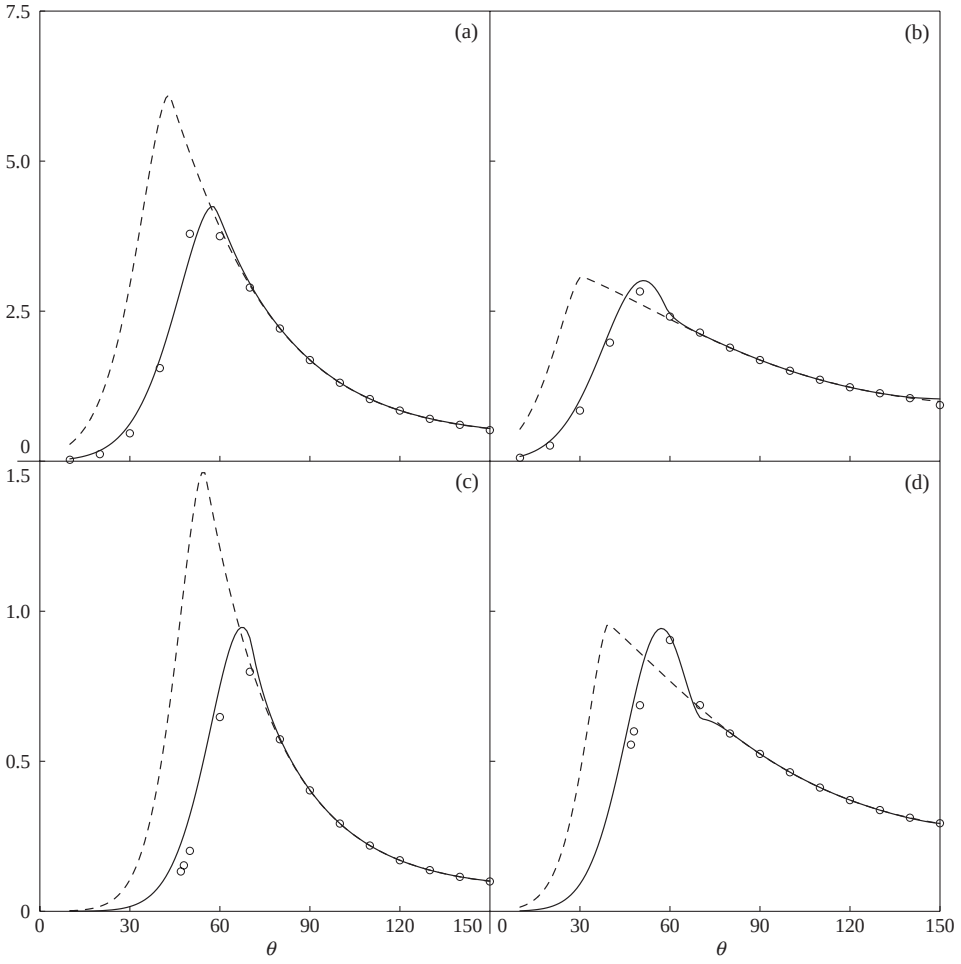

Fig. 9. As Fig. 8 but for $St = 1$.

5. Connection to ray theory

The comparisons of the previous section show that, for parallel round jets, the asymmetric, high-frequency approximation is in good agreement with the exact Lilley's equation Green function over a wide range of Strouhal numbers. One would like to demonstrate a similar level of agreement between the exact and high-frequency asymptotic solutions for more general mean flows. Unfortunately, when the mean flow is neither axisymmetric nor parallel, the problem governing the acoustic propagation can no longer be reduced to a system of linear ordinary differential equations by Fourier analysis and an asymptotic analysis of the type described in Section 3 is no longer possible. Nevertheless, analytic progress can still be made for more general mean flows by considering the high-frequency limit. The corresponding asymptotic solutions are then described in terms of the ray theory of acoustics [3,4].

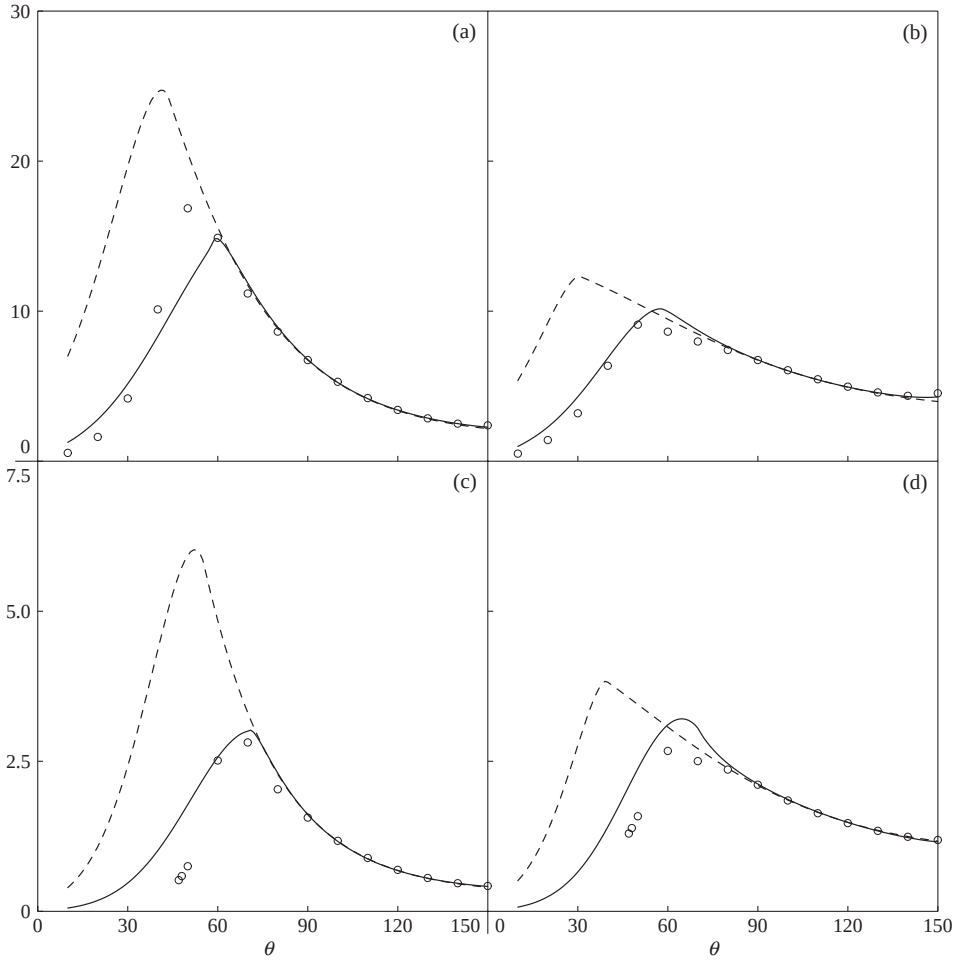

Fig. 10. As Fig. 8 but for $St = 0.5$.

The ray-theory solution of Eq. (4) for the uni-directional transversely sheared mean flow (1) is summarized in Appendix C. The connection between the approximation (C.18) and those presented in Section 3 is revealed by specializing the former result to an axisymmetric mean flow as done by Goldstein [3]. Introducing the mean-flow profiles $M(r)$ and $a(r)$ into Eq. (C.19) shows that $rs^{(\varphi)}$ is constant along each ray. If Eqs. (C.11) and (C.12) are then used to eliminate θ_∞ in favor of θ in the remaining equations, they become, to the required order of accuracy,

$$\left.\begin{aligned} \dot{r} = \pm\left[Q(r|v_\star) + \frac{R_\infty - R}{R}\cos\theta\cot\theta\right], \quad r^2\dot{\varphi} = v_\star, \\ \dot{S}_\perp = v_\star\dot{\varphi} + Q^2(r|v_\star) - \sin^2\theta, \end{aligned}\right\} \tag{32}$$

which must be solved subject to

$$r = r_s, \quad \varphi = \varphi_s, \quad S_\perp = 0$$

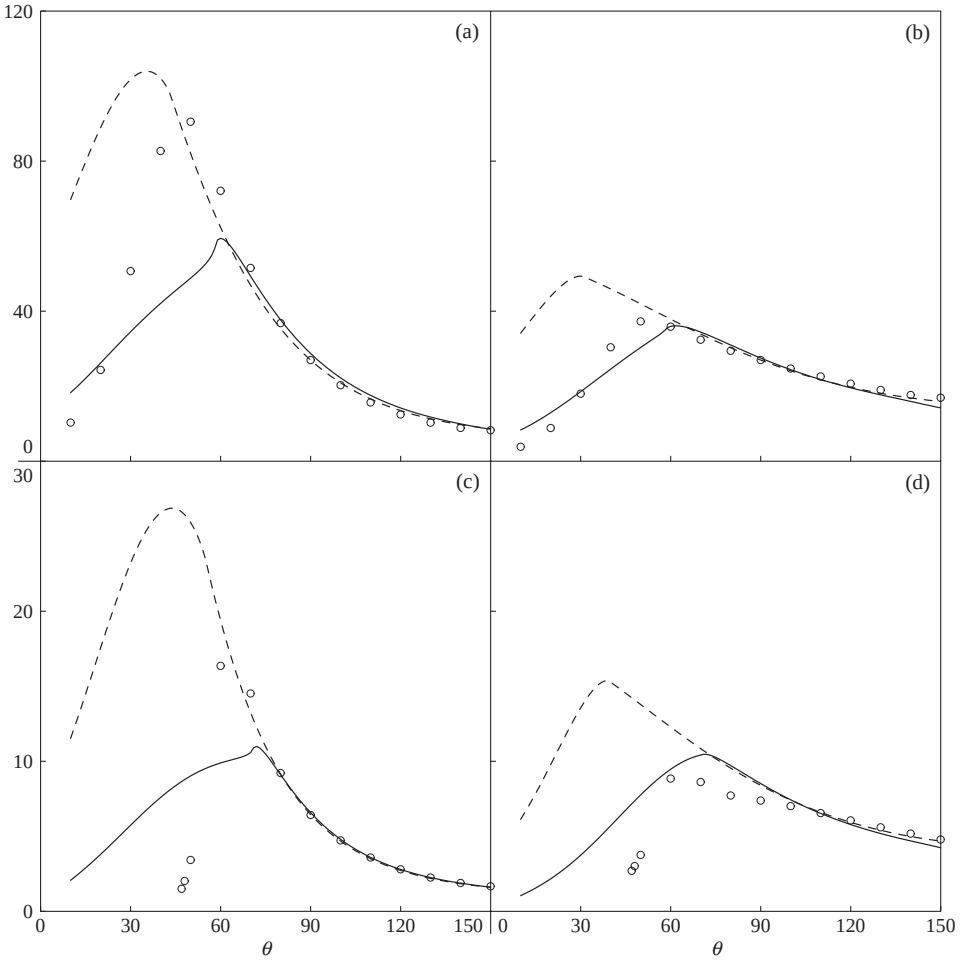

Fig. 11. As Fig. 8 but for $St = 0.25$.

at $\tau = 0$, where $v_\star \equiv r_s q_s \sin(\lambda - \varphi_s) = rs^{(\varphi)}$,

$$rQ(r|v_\star) \equiv \sqrt{r^2 q^2 - v_\star^2}, \tag{33}$$

a dot denotes differentiation with respect to the ray parameter τ and use has been made of Eq. (C.16) in arriving at the definition of $v_\star$. The order $1/R$ term in the $\dot{r}$ equation is retained because it leads to an order-one contribution in the farfield behavior of $S_\perp$. The branch cuts of Q are specified below. For the present, attention will be restricted to the case where $v_\star$ is purely real which, it turns out, implies $Q^2 \geqslant 0$ along the rays. A necessary (but not sufficient) condition for $v_\star$ to be purely real is that the source be located such that $q_s^2 \geqslant 0$.

The choice of sign in the $\dot{r}$ equation of Eqs. (32) is a function of the initial condition,

$$\dot{r} = q_s \cos(\lambda - \varphi_s) \quad \text{at} \quad \tau = 0,$$

as well as the number of zeroes of Q encountered along a ray trajectory $r(\tau)$. It is assumed here (in agreement with the turning-point assumptions made in Appendices A and B) that rQ is a monotonically increasing function of r with at most one simple zero. rQ will then be non-zero and r will increase monotonically with τ for rays initially directed away from the jet centerline, i.e., $-\pi/2<\lambda-\varphi_s<\pi/2$. These solutions, for which the positive sign in Eqs. (32) applies, will be referred to as *direct* rays. For rays initially directed toward the jet centerline, i.e. $\pi/2<\lambda-\varphi_s<3\pi/2$, but which eventually reach the farfield, r initially decreases with increasing τ until $r=r_\delta$ where Q vanishes. Once this occurs, r begins to increase with τ and the sign in Eqs. (32) must change from negative to positive. These solutions will be referred to as *indirect* rays.

In view of the preceding discussion, the solutions to Eqs. (32) can be written as

$$\Delta\varphi=\varphi-\varphi_s=\left(\int_{r_\delta}^{\infty}\mp\int_{r_\delta}^{r_s}\right)\frac{v_\star\,\mathrm{d}r}{r^2Q(r|v_\star)}, \tag{34}$$

$$S_\perp=v_\star\Delta\varphi+\zeta(r|v_\star)\mp\zeta(r_s|v_\star)-R\sin^2\theta-R_\infty+R, \tag{35}$$

where

$$\zeta(r|v_\star)\equiv\int_{r_\delta}^{r}Q(r|v_\star)\,\mathrm{d}r,\quad Q^2(r_\delta|v_\star)=0, \tag{36}$$

and the upper (lower) signs in Eqs. (34) and (35) apply to the direct (indirect) rays. Notice that r_δ cancels out of both the $\Delta\varphi$ and $S_\perp$ solutions when the upper set of signs is chosen. Substituting these results into Eq. (C.18) yields

$$\mathscr{R}_\omega\sim\left[\pm r_sQ(r_s|v_\star)\frac{\partial\varphi}{\partial v_\star}\right]^{-1/2}\mathrm{e}^{\mathrm{i}k_0[v_\star\Delta\varphi+\zeta(r|v_\star)\mp\zeta(r_s|v_\star)-R\sin^2\theta]} \tag{37}$$

as $k_0,R\to\infty$, where $\mathrm{d}v_\star=\pm r_sQ(r_s|v_\star)\,\mathrm{d}\lambda$ follows from the definition of $v_\star$.

Since the results of Appendix C implicitly assume an acoustic field of order $1/k_0$ length scale in *all* directions, a close connection between Eq. (37) and the asymmetric approximation (21) is expected. An explicit demonstration of that connection may seem unnecessary in light of the leading order, large-k_0 approximation of the asymmetric ring-source directivity described in the preceding section. However, like the ring-source approximation, Eq. (37) becomes unbounded whenever θ and $\Delta\varphi$ are such that the bracketed quantity vanishes and the formalism introduced in demonstrating the connection between Eqs. (21) and (37) provides the mathematical apparatus needed to overcome this breakdown.

The Poisson sum formula [14] is used to rewrite Eq. (21) as

$$\mathscr{R}_\omega\sim\sum_{m=-\infty}^{+\infty}\int_{-\infty}^{+\infty}\left[2k_0\frac{\sqrt{-\eta(r_s|v)}}{r_sQ(r_s|v)}\right]^{1/2}\mathrm{Ai}[\eta(r_s|v)]\mathrm{e}^{\mathrm{i}k_0[\alpha_mv+\zeta(r|v)-R\sin^2\theta]}\,\mathrm{d}v, \tag{38}$$

as $k_0,R\to\infty$, where $\alpha_m\equiv\Delta\varphi+2\pi m$,

$$\eta(r|v)\equiv-\left[\frac{3}{2}k_0\zeta(r|v)\right]^{2/3},$$

and $Q(r|v)$ and $\zeta(r|v)$ are given by Eqs. (33) and (36) with $v_\star$ replaced by v.

Since the argument of the square root in Eq. (33) can now be negative (or even complex when the v integration of Eq. (38) is performed in the complex plane), the branch cuts of Q must be made explicit. In the present context, it is clear that Q is simply a generalization of the function Q_n defined by Eq. (16) where the square root was *chosen* so that it has a positive imaginary part for negative (real) arguments. The appropriate generalization of this choice to arbitrary values of v is

$$rQ(r|v) = \sqrt{|r^2q^2 - v^2|}\ \mathrm{e}^{\mathrm{i}[\arg(rq-v)+\arg(rq+v)]/2} \quad \text{with} \quad -\tfrac{1}{2}\pi \leqslant \arg(rq \pm v) < \tfrac{3}{2}\pi. \tag{39}$$

The branch cuts of $Q(r_s|v)$ in the complex v plane are shown in Fig. 12. It is worth noting here that

$$\lim_{v^2 \to r_s^2 q_s^2} \frac{\sqrt{-\eta(r_s|v)}}{r_s Q(r_s|v)} = [k_0 \mathscr{P}(r_s)]^{1/3},$$

where $\mathscr{P}(r) \equiv 1/r(r^2q^2)'$, which shows that the integrand in Eq. (38) remains bounded at the branch points of $Q(r_s|v)$.

The integral in Eq. (38) is evaluated asymptotically in the limit $k_0 \to \infty$ using the method of steepest descents [11] which requires making the k_0 dependence of the integrand explicit. The Airy function Ai can be replaced with its large argument behavior along the entire real v axis except in the small order $k_0^{-2/3}$ neighborhoods of the branch points $\pm r_s q_s$. Thus

$$\mathscr{R}_\omega \sim \begin{cases} \mathscr{R}_\omega^{(-)} - \mathrm{i}\mathscr{R}_\omega^{(+)} + \mathscr{R}_\omega^{(\times)} & \text{for } q_s^2 > 0, \\ \mathscr{R}_\omega^{(-)} & \text{for } q_s^2 < 0 \end{cases} \tag{40}$$

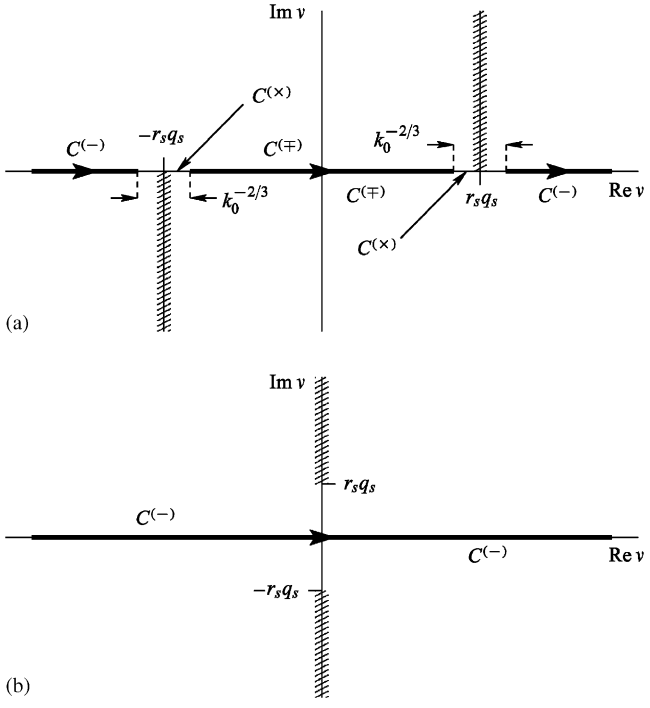

Fig. 12. Branch cuts of $Q(r_s|v)$ in the complex v plane. (a) $q_s^2 > 0$, $C^{(+)}$ lies between $\pm r_s q_s$ where it overlaps $C^{(-)}$; (b) $q_s^2 < 0$.

as $k_0, R \to \infty$, where

$$\mathscr{R}_\omega^{(\mp)} \equiv \sum_{m=-\infty}^{+\infty} \int_{C^{(\mp)}} \left[\frac{\mathrm{i}k_0}{2\pi r_s Q(r_s|v)}\right]^{1/2} \mathrm{e}^{\mathrm{i}k_0[\alpha_m v + \zeta(r|v) \mp \zeta(r_s|v) - R\sin^2\theta]}\,\mathrm{d}v, \tag{41}$$

and $\mathscr{R}_\omega^{(\times)}$ is given by the right-hand side of Eq. (38) but with the integration done over the contour $C^{(\times)}$. The contours $C^{(-)}$, $C^{(+)}$ and $C^{(\times)}$ are shown in Fig. 12.

For the present, it will be supposed that the dominant behavior of Eq. (38) is *not* determined by $\mathscr{R}_\omega^{(\times)}$. This exceptional case is considered in the following section. Applying the method of steepest descents to Eq. (41) yields

$$\mathscr{R}_\omega^{(\mp)} \sim \sum_{v_\star} \left[r_s Q(r_s|v_\star)\left|\frac{\partial\psi}{\partial v_\star}\right|\right]^{-1/2} \mathrm{e}^{\mathrm{i}(\beta+\pi/4)} \mathrm{e}^{\mathrm{i}k_0[\alpha_{m_\star} v_\star + \zeta(r|v_\star) \mp \zeta(r_s|v_\star) - R\sin^2\theta]}, \tag{42}$$

as $k_0 \to \infty$, where

$$-\tfrac{1}{2}\pi < \beta \equiv -\arg\left[(\mathrm{i}\partial\psi/\partial v_\star)^{1/2}\right] \leqslant \tfrac{1}{2}\pi,$$

$m_\star$ and $v_\star$ are determined by the saddle-point condition

$$\alpha_{m_\star} = \Delta\varphi + 2\pi m_\star = \psi(v_\star) \equiv \left(\int_{r_\delta}^{\infty} \mp \int_{r_\delta}^{r_s}\right) \frac{v_\star\,\mathrm{d}r}{r^2 Q(r|v_\star)}, \tag{43}$$

and the ★ subscript is reused in order to emphasize the connection with the ray-theory solution.

It is immediately evident that the ray solution (34) and the saddle-point condition (43) are merely different versions of the same relation. The latter result determines $v_\star$ as a, possibly multi-valued, function of $\Delta\varphi$. Multiple solutions for $v_\star$ at a fixed $\Delta\varphi$ are accounted for by the summation in Eq. (42) and indicate different rays reaching the same farfield observation point. The ray solution (34) determines $\Delta\varphi$ as a *single-valued* function of $v_\star$ so no special treatment is needed for rays that reach the same farfield position. The $2\pi m_\star$ factor in Eq. (43) allows for the possibility that ψ falls outside the range $[-\pi, +\pi]$.

Eqs. (34) and (43) also imply that $\partial\psi/\partial v_\star = \partial\varphi/\partial v_\star$. If $v_\star$ is purely real as assumed when deriving Eq. (37), ψ is also purely real and the amplitude factor in Eq. (42) can be rewritten as

$$\left[r_s Q(r_s|v_\star)\left|\frac{\partial\psi}{\partial v_\star}\right|\right]^{-1/2} \mathrm{e}^{\mathrm{i}(\beta+\pi/4)} = \left[r_s Q(r_s|v_\star)\frac{\partial\psi}{\partial v_\star}\right]^{-1/2}.$$

It then follows that $\mathscr{R}_\omega^{(-)}$ corresponds to the direct-ray solution given by the upper signs in Eq. (37) and the indirect-ray solution will correspond to $-\mathrm{i}\mathscr{R}_\omega^{(+)}$ provided

$$\left[-r_s Q(r_s|v_\star)\frac{\partial\varphi}{\partial v_\star}\right]^{-1/2} = \left[r_s Q(r_s|v_\star)\frac{\partial\varphi}{\partial v_\star}\right]^{-1/2} \mathrm{e}^{-\mathrm{i}\pi/2}.$$

The above condition removes the ambiguity in the phase of Eq. (37) when the lower signs are taken. The $-\pi/2$ phase shift is a consequence of the indirect ray having passed through the caustic at $r = r_\delta$ before reaching the far field. The shift is left undetermined in the ray-theory solution described in Appendix C and, in general, must be obtained through a local analysis near the caustic [15].

The above results clearly establish the connection between the asymmetric, high-frequency solution (21) and the ray-theory solution (37) when $v_\star$ is purely real. Since the location in the complex v plane of the saddle point determined by Eq. (43) is not restricted (other than as required by the method of steepest descents), Eqs. (40) and (42) show how Eq. (37) can be generalized to complex rays. The technique of applying the method of steepest descents to a classical high-frequency solution in order to guide the generalization of a ray-theory result to complex rays is well known [16,17]. Less well known are the methods for developing a complex ray theory when no classical high-frequency solution is available as, for example, in the case of the uni-directional, transversely sheared, mean flow considered in Appendix C. A survey of available approaches for doing just that is given by Chapman et al. [18].

6. Evaluation of ray-theory solution

In arriving at the large-k_0 approximation of $\mathscr{R}_\omega^{(\mp)}$ given by Eq. (42), it was implicitly assumed that the integrand in Eq. (41) can be analytically continued into the complex v plane so as to allow integration along a contour that is (at least locally) coincident with the steepest descent paths intersecting at $v_\star$. When $v_\star$ is complex, care must be taken during the evaluation of Eq. (42) because r_δ is then also complex and the integration of Q in the definition of ζ must be done along a contour in the complex r plane. For each point along that contour, Q has branch cuts in the v plane determined by Eq. (39). The r-integration contour must therefore be chosen such that these branch cuts leave a region of analyticity in the complex v plane that contains both $v_\star$ and the real axis. Fig. 13 shows example contours in the complex r plane used for the evaluation of $\zeta(r|v_\star) + \zeta(r_s|v_\star)$ and $\zeta(r|v_\star) - \zeta(r_s|v_\star)$ as well as the corresponding regions of analyticity in the complex v plane.

Fig. 14 contains a plot of the saddle point $v_\star$ determined from Eq. (43) as a function of polar angle θ for $\Delta\varphi = 60°$, $r_s = 0.75$ and the mean flow given by Eqs. (25) and (27) with $M_J = 0.9$. The direct (indirect) ray solutions, which correspond to the upper (lower) signs in Eq. (43), are indicated by a $\triangle$ ($\square$). The real and imaginary parts of $v_\star$ are denoted by the open and closed symbols respectively.

The figure shows that the complex solutions for $v_\star$ are confined to the range $\theta \lesssim 39.5°$. These solutions describe the so-called zone of silence where a significant reduction in the sound radiated to the far field results from an exponential decay in $\mathscr{R}_\omega$. Notice that the boundary of the zone of silence does *not* coincide with the value $\theta \approx 30.67$ where $q_s^2 = 0$ (cf. Fig. 2(b)). Just outside the zone of silence is a range of θ where multiple (real) solutions for $v_\star$ are found. These multiple solutions occur when different rays reach the same farfield observation point and give rise to ray-interference effects which can be either constructive or destructive depending on the relative phases of the solutions. The ray-interference region extends to $\theta \approx 58$ beyond which q^2 has no turning points (cf. Fig. 2(b)) and only direct-ray solutions are found.

Also shown in Fig. 14 is the location of the branch point $r_s q_s$ along the real v axis. The real part of $v_\star$ intersects this curve at $\theta \approx 37.5°$ with the result that the solution type changes from a complex direct ray ($\theta \lesssim 37.5°$) to a complex indirect ray ($\theta \gtrsim 37.5°$). The change in solution type is a consequence of the phase shift in $Q(r_s|v_\star)$ that occurs as $v_\star$ crosses the branch cut issuing from

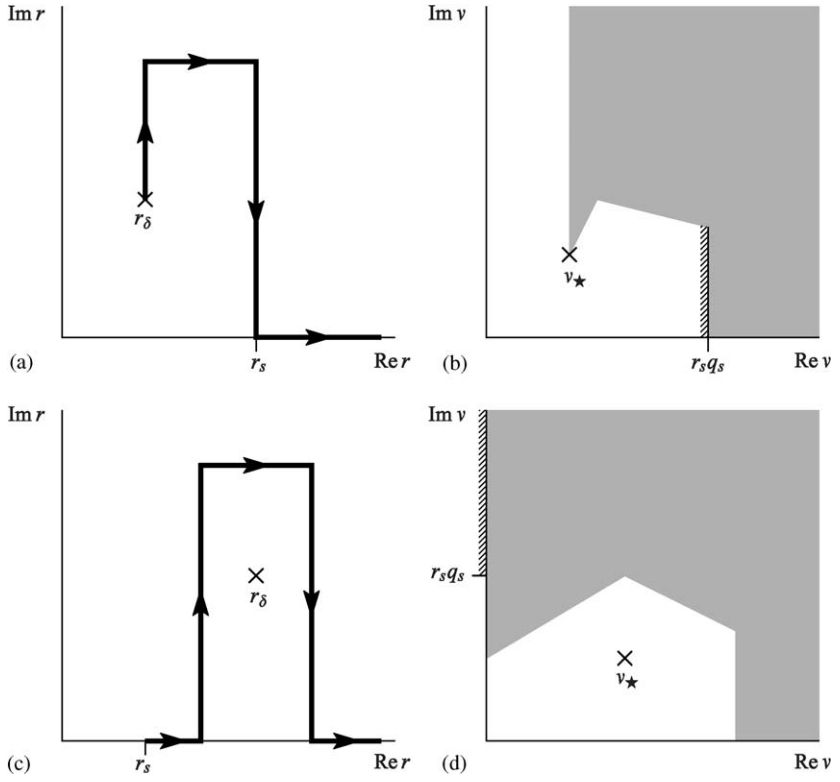

Fig. 13. Contours in the complex r plane (a, c) and corresponding regions in the complex v plane (b,d). Shaded areas indicate location of branch cuts of $Q(r|v)$ along indicated r contours. (a, b) pertain to $\zeta(r|v_\star)+\zeta(r_s|v_\star)$ when $q_s^2>0$; (c, d) pertain to $\zeta(r|v_\star)-\zeta(r_s|v_\star)$ when $q_s^2<0$.

$r_s q_s$ (cf. Fig. 12(a)). The asymptotic approximation (42) remains valid for $v_\star$ arbitrarily close to the branch cut (but outside the order $k_0^{-2/3}$ neighborhood of $r_s q_s$) because the contribution to the large-k_0 behavior of Eq. (41) obtained by deforming the v-integration contour around the branch point is of higher order.

The purely real solutions for $v_\star$ are also affected by an encounter with the $r_s q_s$ curve with the result that the indirect-ray solution ($\theta \lesssim 42^\circ$) changes to a direct-ray solution ($\theta \gtrsim 42^\circ$). The change in solution type occurs as r_δ and r_s become coincident and corresponds to the change that occurs in Eq. (34) as $\lambda-\varphi_s$ passes through $\pi/2$. The approximation of $\mathscr{R}_\omega$ given by Eq. (42) becomes invalid near this point because $v_\star$ moves into the order $k_0^{-2/3}$ neighborhood of a $Q(r_s|v_\star)$ branch point. The dominant behavior of Eq. (38) is then determined by $\mathscr{R}_\omega^{(\times)}$ rather than $\mathscr{R}_\omega^{(-)}$ or $\mathscr{R}_\omega^{(+)}$. The appropriate asymptotic behavior of $\mathscr{R}_\omega$ is found by applying the method of steepest descents to Eq. (38), where the integration is done over the contour $C^{(\times)}$, with the result that

$$\mathscr{R}_\omega^{(\times)} \sim \left[\frac{r_s Q(r_s|\tilde{v})}{4\pi\sqrt{-\eta(r_s|\tilde{v})}}\left|\frac{\partial\tilde{\psi}}{\partial\tilde{v}}\right|\right]^{-1/2} \mathrm{Ai}[\eta(r_s|\tilde{v})]\mathrm{e}^{\mathrm{i}\tilde{\beta}}\mathrm{e}^{\mathrm{i}k_0[\Delta\varphi\tilde{v}+\zeta(r|\tilde{v})-R\sin^2\theta]}, \tag{44}$$

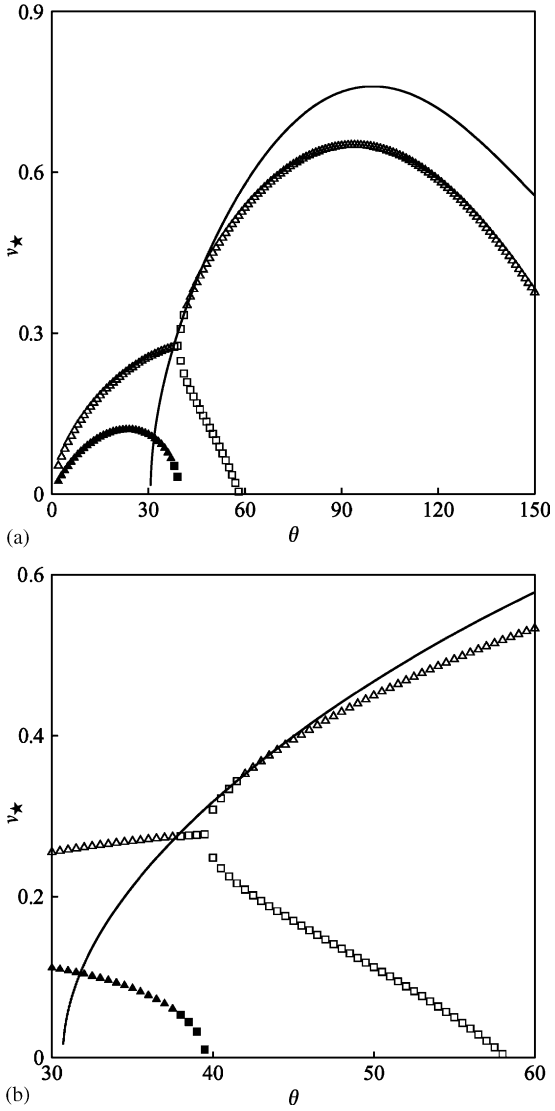

Fig. 14. (a) Saddle points $v_\star$ for an isothermal jet with $r_s = 0.75$ and $\Delta\varphi = 60^\circ$, (b) detail. Open symbols, Re $v_\star$; closed symbols, Im $v_\star$; $\triangle$, direct-ray solution; $\square$, indirect-ray solution; solid line, Re $r_s q_s$.

as $k_0 \to \infty$, where

$$-\tfrac{1}{2}\pi < \tilde{\beta} \equiv -\arg[(\mathrm{i}\partial\tilde{\psi}/\partial\tilde{v})^{1/2}] \leqslant \tfrac{1}{2}\pi, \tag{45}$$

and $\tilde{v}$ is determined by the saddle-point condition

$$\Delta\varphi = \tilde{\psi}(\tilde{v}) \equiv \int_{r_\delta}^{\infty} \frac{\tilde{v}\,\mathrm{d}r}{r^2 Q(r|\tilde{v})}. \tag{46}$$

Fig. 14 reveals another change in solution type which also leads to a local breakdown in the large-k_0 approximation given by Eq. (42). This occurs at the zone of silence boundary $\theta \approx 39.5^\circ$

where the complex indirect-ray saddle point changes into a pair of real indirect-ray solutions. At the point of bifurcation, $v_\star$ becomes a saddle point of higher-order for which

$$\frac{\partial \psi}{\partial v_\star} = 0, \tag{47}$$

with the consequence that the right-hand side of Eq. (42) becomes unbounded. Eq. (47) implies a zero in the Jacobian determinant J introduced in Appendix C and therefore the appearance of a caustic [3]. The breakdown is restricted to indirect-ray solutions as they are the only ones that encounter a caustic before reaching the far field.

An expression for $\partial\psi/\partial v_\star$ can be derived by using Eq. (39) and the defining equation for r_δ to show that

$$\frac{\partial}{\partial v_\star}\left[\frac{v_\star}{r^2 Q(r|v_\star)}\right] = \frac{1+2v_\star^2 r\mathscr{P}'(r)}{r^2 Q(r|v_\star)} - \frac{\partial}{\partial r}\left[\frac{2v_\star^2 \mathscr{P}(r)}{rQ(r|v_\star)}\right],$$

$$\frac{\partial r_\delta}{\partial v_\star} = 2v_\star r_\delta \mathscr{P}(r_\delta),$$

where $\mathscr{P}(r) \equiv 1/r(r^2q^2)'$. Using these results when differentiating Eq. (43) with respect to $v_\star$ leads to

$$\frac{\partial \psi}{\partial v_\star} = \left(\int_{r_\delta}^{\infty} \mp \int_{r_\delta}^{r_s}\right)\frac{1+2v_\star^2 r\mathscr{P}'(r)}{r^2 Q(r|v_\star)}\,\mathrm{d}r \pm \frac{2v_\star^2 \mathscr{P}(r_s)}{r_s Q(r_s|v_\star)}, \tag{48}$$

where the singularity at $r = r_\delta$ is integrable.

A large-k_0 approximation of $\mathscr{R}_\omega^{(+)}$ can be constructed when the saddle point $v_\star$ approaches a zero of $\partial\psi/\partial v_\star$ by using the procedure outlined in appendix G of Ref. [19]. The integrand is expanded about the midpoint $\bar{v}$ rather than the saddle point $v_\star$ when applying the method of steepest descents where $\bar{v}$ is determined by

$$\frac{\partial}{\partial v}\psi(v) = 0, \quad \text{at} \quad v = \bar{v}.$$

Notice that, in view of Eq. (48), $\bar{v}$ is independent of $\Delta\varphi$. The resulting asymptotic approximation is

$$\mathscr{R}_\omega^{(+)} \sim \left[\frac{\mathrm{i}2\pi k_0}{r_s Q(r_s|\bar{v})}\right]^{1/2}\left[\frac{k_0}{2}\left|\frac{\partial^2\psi}{\partial \bar{v}^2}\right|\right]^{-1/3} \mathrm{Ai}(\bar{\eta})\mathrm{e}^{\mathrm{i}\bar{\beta}}\mathrm{e}^{\mathrm{i}k_0[\Delta\varphi\bar{v}+\zeta(r|\bar{v})+\zeta(r_s|\bar{v})-R\sin^2\theta]} \tag{49}$$

as $k_0 \to \infty$, where

$$-\tfrac{1}{3}\pi < \bar{\beta} \equiv -\arg[(\partial^2\psi/\partial\bar{v}^2)^{1/3}] \leqslant \tfrac{1}{3}\pi, \quad \bar{\eta} \equiv -k_0[\psi(\bar{v}) - \Delta\varphi]\left[\frac{k_0}{2}\left|\frac{\partial^2\psi}{\partial\bar{v}^2}\right|\right]^{-1/3}\mathrm{e}^{\mathrm{i}\bar{\beta}},$$

and $\psi(\bar{v})$ is given by Eq. (43) with $v_\star$ replaced by $\bar{v}$.

Fig. 15 is a plot of $|\mathbb{G}_\omega/\mathscr{G}_\omega|$ as a function of polar angle θ for Strouhal number $St = 2$ and $\Delta\varphi = 60^\circ$. The solid line corresponds to the asymmetric high-frequency approximation (21). The dotted line corresponds to the ray-theory solution given by Eqs. (40) and (43). Results based on the near-branch-point solution (44) and the near-caustic solution (49) are indicated by the dot-dashed and dot-dot-dot-dashed lines respectively. The curves were computed using the same mean flow and source position as Fig. 14.

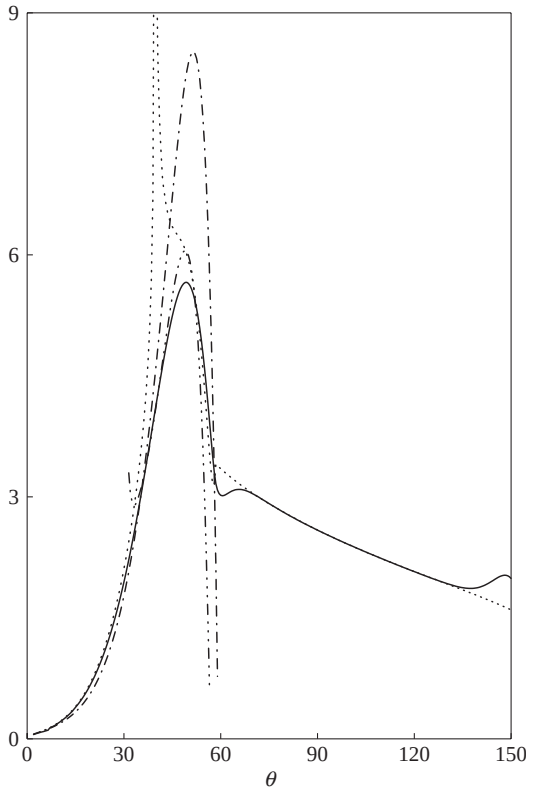

Fig. 15. $|\mathbb{G}_\omega/\mathscr{G}_\omega| \times 10^4$ for an isothermal jet with $r_s = 0.75$, $\Delta\varphi = 60^\circ$ and $St = 2$. Solid line, asymmetric approximation; dotted line, ray-theory solution; dot-dashed line, near-branch-point solution; dot-dot-dot-dashed line, near-caustic solution.

Comparing the dotted and solid curves shows that the ray solution is in good agreement with the asymmetric approximation over most of the θ range including $\theta \lesssim 30^\circ$ which is well inside the zone of silence where the rays are complex. The discrepancy near $\theta = 58^\circ$ is most likely due to the failure of the ray-theory solution to correctly describe the disappearance of the indirect-ray contribution (cf. Fig. 14). The ray-theory result could probably be improved by constructing a local solution that accounts for the higher order zero in Q that emerges for the indirect-ray solution near $\theta = 58^\circ$. A similar explanation likely applies for the discrepancy near $\theta = 150^\circ$ since an additional indirect-ray solution (with $m_\bigstar = -1$) appears in the range $\theta \gtrsim 150^\circ$.

Fig. 15 also shows that the ray solution breaks down at the zone of silence boundary $\theta \approx 39.5^\circ$ as expected. It is interesting to note that Eq. (42) remains bounded (although not in particularly good agreement with the asymmetric approximation) at $\theta \approx 42^\circ$ where $v_\bigstar$ equals the branch point value $r_s q_s$ because, as can be shown from Eq. (48),

$$\lim_{v_\bigstar^2 \to r_s^2 q_s^2} r_s Q(r_s|v_\bigstar) \frac{\partial \psi}{\partial v_\bigstar} = \pm 2 r_s^2 q_s^2 \mathscr{P}(r_s),$$

where again the upper (lower) sign corresponds to the direct (indirect) ray solution.

Comparing the dot-dashed, dot-dot-dot-dashed and solid curves shows that the local solutions (44) and (49) bring the ray-theory result into closer agreement with the asymmetric approximation and hence the exact solution in their respective regions of applicability. In the range $35^\circ < \theta < 50^\circ$, the near-caustic solution (dot-dot-dot-dashed line) yields better agreement with the asymmetric approximation than does the near-branch-point solution. One might then expect that a composite solution formed from Eqs. (40) and (43) together with the near-caustic solution (49) should produce good agreement with the asymmetric approximation over the ranges of θ and $\Delta\varphi$ of interest. However, as $\Delta\varphi$ decreases, the near-branch-point solution becomes the better approximation in the vicinity of the zone of silence boundary and a different approach to constructing a composite ray-theory solution will be taken here.

Fig. 16(a) contains a plot of $\bar{\theta}$ as a function of $\Delta\varphi$ where $\bar{\theta}$ is defined as the value of the polar angle θ at which the indirect-ray saddle point satisfies both Eq. (43) and (47), i.e., the value at which $v_\bigstar = \bar{v}$. The $\bar{\theta}$ curve therefore marks the zone of silence boundary in θ–$\Delta\varphi$ space. As $\Delta\varphi \to 0^\circ$, $\bar{\theta}$ approaches 30.67° which is the value of θ at which q_s^2 vanishes. As $\Delta\varphi$ increases, $\bar{\theta}$ also increases indicating that the zone of silence grows as the azimuthal angle between the farfield observation point and the source position increases.

Fig. 16(b) shows plots of the indirect-ray saddle point $v_\bigstar$ (which is equivalent to $\bar{v}$ here) and the location of the branch point $r_s q_s$ along the real v axis as functions of $\Delta\varphi$ at the zone of silence boundary. It is clear from the figure that $\bar{v}$ eventually moves into the order $k_0^{-2/3}$ neighborhood of a $Q(r_s|v_\bigstar)$ branch point as $\Delta\varphi$ becomes sufficiently small. When this occurs, the near-caustic approximation (49) must be reworked in order to account for the presence of both a branch point

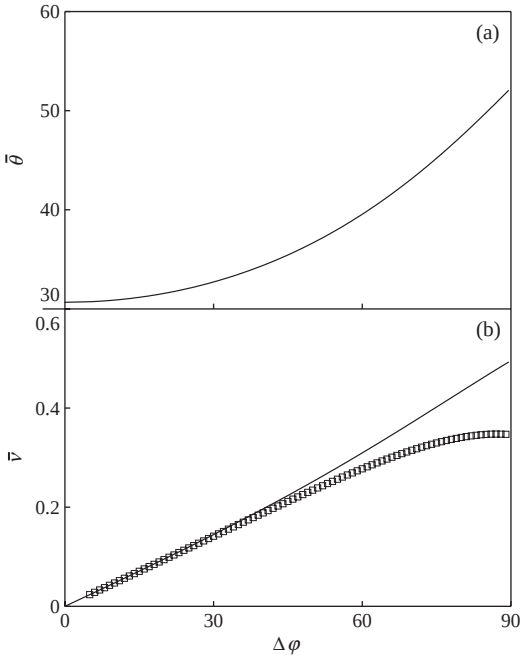

Fig. 16. (a) Polar angle and (b) indirect-ray saddle point evaluated at the zone of silence boundary for an isothermal jet with $r_s = 0.75$. (b) □, midpoint $\bar{v}$; solid line, $\mathrm{Re}\, r_s q_s$.

and a higher order saddle point. Rather than deriving yet another local approximation for $\mathscr{R}_\omega$, the approach taken here is to modify the near-branch-point approximation (44) by shifting the solution to Eq. (45) as follows:

$$\hat{v} = \tilde{v} - \tilde{v}|_{\theta=\bar{\theta}} + \text{sign}(\tilde{v}) r_s q_s|_{\theta=\bar{\theta}}.$$

Thus, $\hat{v}$ coincides with the $Q(r_s|v_\star)$ branch point when $\theta = \bar{\theta}$. If the integrand in Eq. (38) is expanded about $\hat{v}$ rather than $\tilde{v}$ when the method of steepest descents is applied the following expression is obtained:

$$\mathscr{R}_\omega^{(\times)} \sim [\text{right-hand side of (44)}] \times \exp\left[\mathrm{i}\frac{k_0}{2}\frac{(\Delta\varphi - \tilde{\psi})^2}{\partial\tilde{\psi}/\partial\tilde{v}}\right], \tag{50}$$

as $k_0 \to \infty$, where $\tilde{\psi}$ is given by Eq. (46) and all occurrences of $\tilde{v}$ must be replaced by $\hat{v}$ in the above result.

The dot-dashed line in part (b) of Figs. 3–6 corresponds to a composite ray solution for $|\mathbb{G}_\omega/\mathscr{G}_\omega|$ at $\Delta\varphi = 30^\circ$ formed from outer and inner expansions given by Eqs. (40) and (50), respectively. A multiplicative composite form was used when $\eta(r_s|\hat{v}) > 0$ and an additive form otherwise [20]. The figures show that the composite ray solution does an adequate job of extending Eq. (40) through both the branch point and caustic at all St. Apart from the discrepancies near $\theta = 58^\circ$ and 150° discussed above, the composite solution is in fairly good agreement with the asymmetric approximation (and hence the exact result) down to $St = 0.5$. The disagreement near $\theta = 58^\circ$ and 150° tends to spread over a wider θ range as St decreases which supports the conjecture that a local large-k_0 solution could improve the ray-theory result in these regions. It is interesting to note, however, that the composite ray solution gives a better prediction of the exact result near $\theta = 58^\circ$ as St decreases which may indicate that the asymmetric approximation over emphasizes the ray interference effects when St is small. At $St = 0.25$, the composite ray solution continues to accurately predict the asymmetric approximation inside the zone of silence, but, outside the zone of silence, it predicts a more gradual decline in $|\mathbb{G}_\omega/\mathscr{G}_\omega|$ with θ which puts the ray-theory result in better agreement with the exact solution.

A determination of the level of agreement between the exact and high-frequency asymptotic Lilley's equation Green function for more general mean flows would require using the methods of reference [18] to extend the analysis of Appendix C to complex rays and then supplementing those results with local solutions of the sort described in Ref. [15] near any caustics or branch points. Such a program will not be undertaken here. Instead, it may be inferred from the success of the composite ray solution at predicting the asymmetric approximation that the level of agreement between the exact and high-frequency asymptotic solutions for more general mean flows would be similar to that shown in Figs. 3–11 between the exact solution and the asymmetric high-frequency approximation.

7. Conclusions

It has been shown that, for parallel round jets, the asymmetric high-frequency approximation, which applies to sources away from the jet axis, provides the best overall prediction of the exact Lilley's equation Green function and remains accurate for Strouhal numbers as small as 1/2. The

quasi-symmetric high-frequency approximation, which uses a near-axis source assumption, was found to be most successful when applied to the ring-source directivity and gives a good approximation of the exact ring-source result at all Strouhal numbers considered provided the polar angle from the downstream axis is sufficiently large. In this range of angles, an equivalence of the quasi-symmetric and asymmetric ring-source approximations was demonstrated.

The ray-theory solution was shown to be closely connected to the asymmetric high-frequency approximation and this close association was used to guide a generalization of the ray-theory result to complex rays. When combined with appropriate local solutions near the caustic and branch point, the ray-theory solution was found to be in good agreement with the asymmetric approximation and hence the exact result for the Lilley's equation Green function. This finding was used to infer the potential for success of the high-frequency asymptotic Green function for more general (i.e., non-axisymmetric and/or non-parallel) mean flows.

The numerical results presented here apply to stationary sources embedded in a subsonic parallel round jet and are restricted to flow situations where Lilley's equation contains at most one simple turning point. The generalization to multiple and/or higher-order turning points would require modifying the WKB analysis given in Appendix A but this is straight-forward and presents no great difficulty other than algebraic. The only impediment to applying the results of the present analysis to supersonic flows is the possibility of encountering a zero in the denominator of Eq. (24) when the source is located such that $M_s > 1$. This singularity can however be 'removed' with the techniques developed by Ffowcs Williams [21]. Extension to sources convecting in the mean-flow direction can be made by simply introducing an appropriate Galilean transform into Eq. (4).

It was noted that development of a uniformly valid high-frequency asymptotic Green function for more general mean flows would involve extending the ray-theory analysis of Appendix C to complex rays and then supplementing those results with appropriate local solutions near any caustics or branch points. The complications associated with complex rays may however be significantly lessened by simply accounting for mean-flow divergence effects. Durbin [22] notes that jet spreading tends to eliminate the zone of silence by producing progressively flatter mean-velocity profiles that are less effective at deflecting radiated sound waves away from the jet axis. In any event, the ray-theory solution may not lend itself well to implementation in a jet-noise prediction scheme because the Green function is given in terms of the initial ray direction rather than the orientation of the farfield observation point. A similar discord between desired and computed solution forms arises in the exact order-one frequency problem but has recently been overcome for both axisymmetric [13] and non-axisymmetric [1] mean flows by recasting the problem in terms of the adjoint Green function. Interchanging the source and observation points allows the Green function for all source locations in the jet that radiate in a given farfield direction to be obtained from a single computation. The adjoint Green function formulation may be similarly helpful in developing a more convenient form for the high-frequency asymptotic solution.

Appendix A. Asymmetric, high-frequency approximation

In this appendix, high-frequency asymptotic solutions for v_1 and v_2 are constructed using the azimuthal wavenumber scaling $n = O(k_0)$. The solution forms are strongly dependent on the

turning points of Eq. (13) which are determined by the zeroes of Q_n^2. It follows from Eq. (16) that

$$Q_n^2 \to \begin{cases} -(n/k_0 r)^2 & \text{as} \quad r \to 0, \\ \sin^2\theta & \text{as} \quad r \to \infty. \end{cases}$$

Therefore, Eq. (13) always has at least one turning point with the current scaling of n.

For isothermal, subsonic jets with monotonically decreasing Mach number profiles, it can be shown [6] that Q_n^2 has at most one simple zero for $0^\circ < \theta \leqslant 90^\circ$. The situation becomes complicated for more general jet profiles and for polar angles in the range $90^\circ < \theta < 180^\circ$ due to the possibility of multiple and/or higher-order turning points which then depend on the detailed shape of the mean-flow profiles. In order to keep the analysis as simple as possible, it will be assumed here (as well as in Appendix B) that Eq. (13) has at most one simple turning point. The present analysis can, if necessary, be extended to more complicated situations by making some straightforward modifications to the results given here.

Let r_δ denote the single n-dependent turning point of Eq. (13), then the general solution

$$v \sim \begin{cases} |Q_n|^{-1/2}(A^- \mathrm{e}^{-\mathrm{i}k_0\zeta_n} + B^- \mathrm{e}^{\mathrm{i}k_0\zeta_n}), & r_\delta - r \gg k_0^{-2/3}, \\ \tilde{A}\,\mathrm{Ai}(\tilde{\eta}_n) + \tilde{B}\,\mathrm{Bi}(\tilde{\eta}_n), & |r - r_\delta| = O(k_0^{-2/3}), \\ |Q_n|^{-1/2}(A^+ \mathrm{e}^{\mathrm{i}k_0\zeta_n} + B^+ \mathrm{e}^{-\mathrm{i}k_0\zeta_n}), & r - r_\delta \gg k_0^{-2/3} \end{cases} \tag{A.1}$$

as $k_0 \to \infty$, follows from WKB theory [11], where

$$\tilde{\eta}_n \equiv \chi(r_\delta - r), \quad \chi \equiv \left(k_0^2 \frac{\mathrm{d}}{\mathrm{d}r} Q_n^2 \bigg|_{r=r_\delta} \right)^{1/3}, \quad \zeta_n(r) \equiv \int_{r_\delta}^{r} Q_n(r)\,\mathrm{d}r,$$

and Ai and Bi denote Airy functions in the notation of Ref. [12]. The constants $A^\pm$, $B^\pm$, $\tilde{A}$ and $\tilde{B}$ are related by

$$2A^- = \left(\frac{\chi}{\pi k_0}\right)^{1/2} \tilde{A} = A^+ \mathrm{e}^{\mathrm{i}\pi/4} + B^+ \mathrm{e}^{-\mathrm{i}\pi/4}, \tag{A.2}$$

$$B^- = \left(\frac{\chi}{\pi k_0}\right)^{1/2} \tilde{B} = A^+ \mathrm{e}^{-\mathrm{i}\pi/4} + B^+ \mathrm{e}^{\mathrm{i}\pi/4}, \tag{A.3}$$

which ensure matching between the limiting forms in Eq. (A.1).

Applying the outgoing-wave condition (14) to Eq. (A.1) shows that $B^+ = 0$. The corresponding solution can then be written as

$$v_1(r) \sim Q_n^{-1/2}(r) A_1^+ \mathrm{e}^{\mathrm{i}k_0\zeta_n(r)},$$

as $k_0 \to \infty$, where attention is restricted to the $r - r_\delta \gg k_0^{-2/3}$ behavior since that is all that is required in Eq. (20).

The bounded condition (15) requires $B^- = 0$. In this case, only the value of the corresponding solution at $r = r_s$ appears in Eq. (20). However, the location of the turning point r_δ relative to r_s varies with both θ and n and it is therefore convenient to express the v_2 solution in the uniformly

valid composite form

$$v_2(r_s) \sim A_2^- \left[4\pi \frac{\sqrt{-\eta_n(r_s)}}{Q_n(r_s)} \right]^{1/2} \mathrm{Ai}[\eta_n(r_s)]$$

as $k_0 \to \infty$, where

$$\eta_n(r) \equiv -\left[\frac{3}{2} k_0 \zeta_n(r) \right]^{2/3},$$

with the cube root defined such that $\eta_n \lessgtr 0$ for $r \gtrless r_\delta$.

Since the Wronskian V is independent of r, the $r - r_\delta \gg k_0^{-2/3}$ behavior of v_1 and v_2 can be used to show that

$$V \equiv v_1 v_2' - v_1' v_2 \sim -\mathrm{i}2k_0 A_1^+ A_2^- \mathrm{e}^{\mathrm{i}\pi/4},$$

as $k_0 \to \infty$. Combining this result with the expressions for $v_1(r)$ and $v_2(r_s)$ given above leads to

$$\frac{v_1(r) v_2(r_s)}{V} \sim \left[\frac{\mathrm{i}\pi}{k_0^2} \frac{\sqrt{-\eta_n(r_s)}}{Q_n(r_s) Q_n(r)} \right]^{1/2} \mathrm{Ai}[\eta_n(r_s)] \mathrm{e}^{\mathrm{i}k_0 \zeta_n(r)}, \tag{A.4}$$

as $k_0 \to \infty$.

Appendix B. Quasi-symmetric, high-frequency approximation

In this appendix, the high-frequency solutions to Eq. (13) are constructed using the azimuthal wavenumber scaling $n = O(1)$. Eqs. (16) and(17) show that $k_0^2 Q_n^2$ and $\mathscr{S}$ then become of equal order as r becomes sufficiently small. The disordering of Eq. (13) is dealt with, as in Ref. [2], by introducing an inner region where

$$\bar{r} \equiv k_0 r = O(1).$$

The corresponding equation for v is given to the required order of accuracy by

$$\bar{r}^2 \frac{\mathrm{d}^2 v}{\mathrm{d}\bar{r}^2} + [\bar{r}^2 q^2(0) - n^2 + \tfrac{1}{4}] v = 0,$$

which has the general solution

$$v \sim \sqrt{\bar{r}} \left[\bar{A} \mathrm{J}_n(\bar{\xi}) + \bar{B} \mathrm{H}_n^{(1)}(\bar{\xi}) \right], \tag{B.1}$$

as $k_0 \to \infty$, where $\bar{\xi} \equiv q(0)\bar{r}$ and J_n and $\mathrm{H}_n^{(1)}$ denote the Bessel and Hankel functions of the first kind respectively.

When r is order one, the solution to Eq. (13) is determined, to the required order of accuracy, by

$$v'' + k_0^2 q^2 v = 0, \tag{B.2}$$

which can, of course, be solved using WKB theory [11]. The particular form of the solution depends on the number and nature of the turning points determined by the zeroes of q^2. As in

Appendix A, it will be assumed here, for simplicity, that the v equation has at most one simple turning point.

First, suppose that Eq. (B.2) has a turning point at $r = r_\sigma \gg 1/k_0$ where the notation r_σ is used to distinguish the zeroes of q^2 from the n-dependent zeroes of Q_n^2. The solution to Eq. (B.2) is then given by Eqs. (A.1), (A.2) and (A.3) with n set equal to zero. Matching that result with Eq. (B.1) as $\bar{r} \to O(k_0)$ (noting that $\bar{\xi}$ is purely imaginary) requires

$$\sqrt{2\pi}A^- = \mathrm{e}^{-\mathrm{i}(k_0\xi_\sigma - n\pi/2)}\bar{A}, \quad \sqrt{2\pi}B^- = -\mathrm{i}2\mathrm{e}^{\mathrm{i}(k_0\xi_\sigma - n\pi/2)}\bar{B},$$

where

$$\xi(r) \equiv \int_0^r q(r)\,\mathrm{d}r,$$

and a subscript σ is used to indicate evaluation at $r = r_\sigma$.

Applying the outgoing-wave condition (14) shows that $B^+ = 0$ from which follows:

$$v_1(r) \sim A_1^+ \left(\frac{\mathrm{i}\pi}{2}\frac{k_0\xi}{q}\right)^{1/2} \mathrm{H}_n^{(1)}(k_0\xi)\mathrm{e}^{-\mathrm{i}(k_0\xi_\sigma - n\pi/2)} \tag{B.3}$$

as $k_0 \to \infty$, where attention is restricted to the $r - r_\sigma \gg k_0^{-2/3}$ behavior since that is all that is required in Eq. (20) and the Hankel function has been introduced (without loss of generality) in order to facilitate the application of Graf's addition theorem [12] in Section 3.

The bounded condition (15) requires $\bar{B} = 0$ and the corresponding expression for $v_2(r_\mathrm{s})$ depends on the location of r_σ relative to r_s. Reasoning that the quasi-symmetric approximation is only appropriate when $r_\mathrm{s} \ll 1$, Balsa [2] employed the simplifying assumption that $r_\sigma - r_\mathrm{s} \gg k_0^{-2/3}$, i.e., that the source is always closer to the jet axis than the turning point. Using this assumption, $v_2(r_\mathrm{s})$ can be expressed as

$$v_2(r_\mathrm{s}) \sim \bar{A}_2 \left(\frac{k_0\xi_\mathrm{s}}{q_\mathrm{s}}\right)^{1/2} \mathrm{J}_n(k_0\xi_\mathrm{s}) \tag{B.4}$$

as $k_0 \to \infty$. It should be noted that for any given value of r_s there will be, in general, a range of θ for which $r_\mathrm{s} > r_\sigma$ and, consequently, for which the above expression is invalid. The implications of this failure are discussed in Section 4 where comparisons with the order-one frequency solution for the reduced Green function are given.

Unlike the situation encountered in Appendix A, it is possible, with the present scaling of n, that the equation governing v has *no* turning points. When this is the case, the solution to Eq. (B.2) is given as

$$v \sim q^{-1/2}(A^+\mathrm{e}^{\mathrm{i}k_0\zeta_0} + B^+\mathrm{e}^{-\mathrm{i}k_0\zeta_0}),$$

as $k_0 \to \infty$. Matching with Eq. (B.1) as $\bar{r} \to O(k_0)$ (noting that $\bar{\xi}$ is now purely real) requires

$$\sqrt{\mathrm{i}2\pi}A^+ = (\bar{A} + 2\bar{B})\mathrm{e}^{-\mathrm{i}n\pi/2}, \quad \sqrt{\mathrm{i}2\pi}B^+ = \mathrm{i}\bar{A}\mathrm{e}^{\mathrm{i}n\pi/2}.$$

Expressions for $v_1(r)$ and $v_2(r_\mathrm{s})$ can be derived by applying the boundary conditions (14) and(15) as done above. It turns out that the final expressions are in exact agreement with those given by Eqs. (B.3) and (B.4) if the convention that $r_\sigma = 0$ when q^2 has no zeroes is adopted.

The r-independent Wronskian V can be evaluated using the $r - r_\sigma \gg k_0^{-2/3}$ behaviors of v_1 and v_2 and is given, for the one- and no-turning point solutions, by

$$V \equiv v_1 v_2' - v_1' v_2 \sim -\mathrm{i}k_0 \left(\frac{\mathrm{i}2}{\pi}\right)^{1/2} A_1^+ \bar{A}_2 \mathrm{e}^{-\mathrm{i}(k_0\xi_\sigma - n\pi/2)},$$

as $k_0 \to \infty$. Combining this result with the expressions for $v_1(r)$ and $v_2(r_\mathrm{s})$ given above leads to

$$\frac{v_1(r)v_2(r_\mathrm{s})}{V} \sim \frac{\mathrm{i}\pi}{2}\left(\frac{\xi_\mathrm{s}\xi}{q_\mathrm{s}q}\right)^{1/2} \mathrm{H}_n^{(1)}(k_0\xi)\mathrm{J}_n(k_0\xi_\mathrm{s}), \tag{B.5}$$

as $k_0 \to \infty$.

Appendix C. Ray-theory approximation

In this appendix, the high-frequency solution to Eq. (4) obtained from ray theory is reviewed. Following the matched asymptotic analysis given by Durbin [4], the solution to Eq. (4) for the uni-directional, transversely sheared mean flow (1) is

$$G_\omega(\mathbf{x}|\mathbf{x}_\mathrm{s}) \sim \Phi(\mathbf{x})\mathrm{A}(\mathbf{x}|\mathbf{x}_\mathrm{s})\mathrm{e}^{\mathrm{i}k_0 S(\mathbf{x}|\mathbf{x}_\mathrm{s})}, \tag{C.1}$$

as $k_0 \to \infty$, where the Eikonal S satisfies

$$\Phi^2 - |\mathbf{s}|^2 = 0, \quad \mathbf{s} \equiv \boldsymbol{\nabla} S, \tag{C.2}$$

the amplitude function A satisfies

$$\boldsymbol{\nabla}\cdot\left[\left(\mathbf{s} + \mathbf{i}\frac{M}{a}\Phi\right)\mathrm{A}^2\right] = 0, \tag{C.3}$$

and here $\Phi \equiv (1 - M\mathbf{i}\cdot\mathbf{s})/a$.

The first order partial-differential equation (C.2) is reduced to the coupled system of ordinary differential equations,

$$\dot{\mathbf{x}} = \mathbf{s} + \mathbf{i}\frac{M}{a}\Phi, \quad \dot{\mathbf{s}} = \tfrac{1}{2}\boldsymbol{\nabla}_\perp(\Phi^2), \quad \dot{S} = \mathbf{s}\cdot\dot{\mathbf{x}}, \tag{C.4}$$

along the rays $\mathbf{x}(\tau)$ by the method of characteristics, where τ is a parameter that varies continuously along the ray, a dot indicates differentiation with respect to τ and $\boldsymbol{\nabla}_\perp$ is the gradient operator in the y–z plane. Eq. (C.4) must be solved subject to initial conditions,

$$\mathbf{x} = \mathbf{x}_\mathrm{s}, \quad \dot{\mathbf{x}} = \sigma_\mathrm{s}\{\cos\mu, \sin\mu\cos\lambda, \sin\mu\sin\lambda\}, \quad S = 0 \tag{C.5}$$

at $\tau = 0$, where the free parameters μ and λ determine the initial ray direction relative to the Cartesian co-ordinate system $\{x, y, z\}$, and it follows from Eqs. (C.2) and (C.4) that

$$\sigma_\mathrm{s}^{-2} = a_\mathrm{s}^2 - M_\mathrm{s}^2\sin^2\mu. \tag{C.6}$$

The amplitude function A is found by solving Eq. (C.3) subject to matching with a near-source solution. It follows from the analysis of Ref. [4] that

$$\mathrm{A}(\mathbf{x}|\mathbf{x}_\mathrm{s}) = \frac{1}{4\pi a_\mathrm{s}\Phi_\mathrm{s}}\left(\frac{\sigma_\mathrm{s}^3\sin\mu}{J}\right)^{1/2}, \tag{C.7}$$

where

$$J \equiv \frac{\partial(x, y, z)}{\partial(\tau, \mu, \lambda)} \tag{C.8}$$

is the Jacobian determinant.

When attention is restricted to the far field, solution (C.1) can be simplified by noting that the rays $\mathbf{x}(\tau)$ become straight lines in the absence of a mean flow. Thus, in the far field, the approximation

$$\mathbf{x} \sim \mathbf{x}_s + R_\infty \{\cos\theta_\infty, \sin\theta_\infty \cos\phi_\infty, \sin\theta_\infty \sin\phi_\infty\} \tag{C.9}$$

can be introduced, where R_∞ is the distance between the farfield observation point and the source position and θ_∞ and ϕ_∞ are the farfield polar and azimuthal angles measured from axes passing through the source position and aligned with the x and y directions respectively. It is important to note that ϕ_∞, θ_∞ and R_∞ are *not* equal to φ, θ and R of Sections 2 and 3 but approach these quantities in the far field, i.e.

$$\phi_\infty \sim \varphi + \frac{r_s}{R}\cos\theta \sin\Delta\varphi + \cdots, \tag{C.10}$$

$$\theta_\infty \sim \theta + \frac{r_s}{R}\cos\theta(1 - \cos\Delta\varphi) + \cdots, \tag{C.11}$$

$$R_\infty \sim R + r_s \sin\theta(1 - \cos\Delta\varphi) + \cdots \tag{C.12}$$

as $R \to \infty$.

It follows from Eqs. (C.2) and (C.4) that $\dot{R}_\infty = 1$ which can then be used when inserting Eq. (C.9) into Eq. (C.8) to obtain

$$J \sim R_\infty^2 \sin\theta_\infty \frac{\partial(\theta_\infty, \phi_\infty)}{\partial(\mu, \lambda)}, \tag{C.13}$$

as $R_\infty \to \infty$. Since Eq. (C.4) implies that the quantity $\mathbf{i}\cdot\mathbf{s}$ is constant along each ray, Eqs. (C.5) and (C.9) show that

$$\mathbf{i}\cdot\mathbf{s} = \frac{a_s^2\sigma_s\cos\mu - M_s}{a_s^2 - M_s^2} = \cos\theta_\infty, \tag{C.14}$$

and furthermore, in view of Eq. (C.6), $\theta_\infty = \theta_\infty(\mu)$ and

$$\sin\theta_\infty \frac{\mathrm{d}\theta_\infty}{\mathrm{d}\mu} = a_s^2\sigma_s^3 \sin\mu. \tag{C.15}$$

An additional consequence of Eq. (C.14) is

$$\sigma_s^2 \sin^2\mu = \Phi_s^2 - \cos^2\theta_\infty, \tag{C.16}$$

which follows directly from the Eikonal equation (C.2). The Eikonal itself has the farfield behavior

$$S \sim R_\infty + S_\perp(\mathbf{x}|\mathbf{x}_s), \tag{C.17}$$

as $R_\infty \to \infty$, where

$$S_\perp \equiv \int_0^\tau (\mathbf{s}\cdot\dot{\mathbf{x}}_\perp - \sin^2\theta_\infty)\,\mathrm{d}\tau$$

remains bounded as $R_\infty \to \infty$ and $\mathbf{x}_\perp = \{y, z\}$ denotes the ray vector in the y–z plane.

Substituting Eqs. (C.15) into Eq. (C.13) and the result into Eq. (C.7) yields the farfield approximation for A which when substituted, together with Eq. (C.17), into Eq. (C.1) leads to Eqs. (18) and (19), where now

$$\mathscr{R}_\omega \sim \left(\frac{\partial\varphi}{\partial\lambda}\right)^{-1/2} \mathrm{e}^{\mathrm{i}k_0(S_\perp + R_\infty - R)}, \tag{C.18}$$

as k_0, $R \to \infty$, and where use has been made of the farfield relations (C.10)–(C.12).

For the purposes of the present investigation, it is convenient to restate Eqs. (C.4) and (C.5) in terms of the cylindrical co-ordinates $\{x, r, \varphi\}$ of Section 2. The ray equations in the y–z plane are then

$$\left.\begin{aligned} &(\dot{r})^2 = \Phi^2 - \cos^2\theta_\infty - s^{(\varphi)^2}, \quad && r\dot{\varphi} = s^{(\varphi)}, \\ &(\dot{rs^{(\varphi)}}) = \tfrac{1}{2}\partial(\Phi^2)/\partial\varphi, && \dot{S}_\perp = rs^{(\varphi)}\dot{\varphi} + (\dot{r})^2 - \sin^2\theta_\infty, \end{aligned}\right\} \tag{C.19}$$

which must be solved subject to

$$r = r_\mathrm{s}, \quad \varphi = \varphi_\mathrm{s}, \quad s^{(\varphi)} = \sigma_\mathrm{s}\sin\mu\sin(\lambda - \varphi_\mathrm{s}), \quad S_\perp = 0$$

at $\tau = 0$, where $rs^{(\varphi)} \equiv \partial S/\partial\varphi$.

References

[1] C.K.W. Tam, N.N. Pastouchenko, Noise from fine-scale turbulence of nonaxisymmetric jets, *American Institute of Aeronautics and Astronautics Journal* 40 (2002) 456–464.

[2] T.F. Balsa, The far field of high frequency convected singularities in sheared flows, with an application to jet-noise prediction, *Journal of Fluid Mechanics* 74 (1976) 193–208.

[3] M.E. Goldstein, High frequency sound emission from moving point multipole sources embedded in arbitrary transversely shear mean flows, *Journal of Sound and Vibration* 80 (1982) 499–522.

[4] P.A. Durbin, High frequency Green function for aerodynamic noise in moving media, Part I: general theory, *Journal of Sound and Vibration* 91 (1983) 519–525.

[5] R. Mani, P.R. Gliebe, T.F. Balsa, High velocity jet noise source location and reduction, FAA-RD-76-79- II, 1978.

[6] M.E. Goldstein, *Aeroacoustics*, McGraw-Hill, New York, 1976.

[7] B.J. Tester, C.L. Morfey, Developments in jet noise modelling—theoretical predictions and comparisons with measured data, *Journal of Sound and Vibration* 46 (1976) 79–103.

[8] J.N. Scott, Propagation of sound waves through a linear shear layer, *American Institute of Aeronautics and Astronautics Journal* 17 (1979) 237–244.

[9] M.E. Goldstein, Aeroacoustics of turbulent shear flows, *Annual Review of Fluid Mechanics* 16 (1984) 263–285.

[10] M.E. Goldstein, An exact form of Lilley's equation with a velocity quadrupole/temperature dipole source term, *Journal of Fluid Mechanics* 443 (2001) 231–236.

[11] C.M. Bender, S.A. Orszag, *Advanced Mathematical Methods for Scientists and Engineers*, McGraw-Hill, New York, 1978.

[12] M. Abramowitz, I.A. Stegun, *Handbook of Mathematical Functions*, National Bureau of Standards, Washington, DC, 1964.

[13] C.K.W. Tam, L. Auriault, Mean flow refraction effects on sound radiated from localized sources in a jet, *Journal of Fluid Mechanics* 370 (1998) 149–174.
[14] G.F. Carrier, M. Krook, C.E. Pearson, *Functions of a Complex Variable*, Hod Books, New York, 1983.
[15] R.N. Buchal, J.B. Keller, Boundary layer problems in diffraction theory, *Communications on Pure and Applied Mathematics* 13 (1960) 85–114.
[16] B.D. Seckler, J.B. Keller, Geometrical theory of diffraction in inhomogeneous media, *Journal of the Acoustical Society of America* 31 (1959) 192–205.
[17] B.D. Seckler, J.B. Keller, Asymptotic theory of diffraction in inhomogeneous media, *Journal of the Acoustical Society of America* 31 (1959) 206–216.
[18] S.J. Chapman, J.M.H. Law, J.R. Ockendon, R.H. Tew, On the theory of complex rays, *Society for Industrial and Applied Mathematics Review* 41 (1999) 417–509.
[19] D.S. Jones, *Acoustic and Electromagnetic Waves*, Clarendon Press, Oxford, 1986.
[20] M. Van Dyke, *Perturbation Methods in Fluid Mechanics*, Parabolic Press, Stanford, 1975.
[21] J.E. Ffowcs Williams, The noise from turbulence convected at high speed, *Philosophical Transactions of the Royal Society of London. Series A* 255 (1963) 469–503.
[22] P.A. Durbin, High frequency Green function for aerodynamic noise in moving media, Part II: noise from a spreading jet, *Journal of Sound and Vibration* 91 (1983) 519–525.